UNIVERSITY OF OKLAHOMA

GRADUATE COLLEGE

EFFECT OF FIBER CONTENT ON TENSILE STRENGTH OF NON-PROPRIETARY ULTRA-HIGH PERFORMANCE CONCRETE

A THESIS

SUBMITTED TO THE GRADUATE FACULTY

in partial fulfillment of the requirements for the

Degree of

MASTER OF SCIENCE

By

RICHARD CAMPOS
Norman, Oklahoma
2020

EFFECT OF FIBER CONTENT ON TENSILE STRENGTH OF NON-PROPRIETARY ULTRA-HIGH PERFORMANCE CONCRETE

A THESIS APPROVED FOR THE
SCHOOL OF CIVIL ENGINEERING AND ENVIRONMENTAL SCIENCE

BY THE COMMITTEE CONSISTING OF

Dr. Royce Floyd, Chair

Dr. Musharraf Zaman

Dr. Jeffrey Volz

Table of Contents

List of Tables

List of Figures

Abstract

Ultra-high performance concrete (UHPC) is being used to solve challenging concrete structural applications where conventional concrete would otherwise deteriorate and improved structural properties can be utilized. UHPC is preferred for its high compressive and tensile strengths, which are achieved by a low water-cementitious materials ratio (*w*/*cm*), optimized particle gradation, and adding materials such as silica fume and steel fibers to the matrix. Steel fibers also increase other mechanical properties, such as splitting tensile (indirect tensile) and flexural (modulus of rupture) strengths. The present study uses varying steel fiber contents as well as direct tensile, splitting tensile, compressive and flexural strengths of 60 specimens to develop preliminary empirical models that correlate the direct tensile first crack strength, post-cracking strength, and fiber content with the splitting tensile, flexural (modulus of rupture), and compressive strengths at 28 days for non-proprietary UHPC. The accuracy of the developed models is verified by comparing their predictive capabilities with the actual strengths obtained from the laboratory tests. Literature was surveyed to determine significant information related to this study to develop an advanced understanding of non-proprietary UHPC and correlation modeling. The laboratory experiments that were conducted in this study include flowability, compressive strength, and direct tensile strength tests. Steel fiber contents of 0%, 1%, 2%, 4%, and 6% were considered in this study. Statistical analysis software was used to analyze the strength test results and develop regression models. The root mean square error method was used to analyze the accuracy between the values predicted by the regression models and the actual laboratory values. The regression equations exhibit small errors when compared to the experimental results, which allow for efficient and realistic predictions of the direct tensile and flexural strengths.

1 Introduction

The assessment of the strength capacity of concrete bridges, pavements, and structures is necessary as the structures age and sustain distresses. The stresses that degrade and prematurely crack concrete structures are attributed to traffic-induced stresses, weather, and construction deficiencies due to poor quality control measures. Concrete distresses can lead to costly vehicle repairs, increased maintenance, and rehabilitation. Furthermore, poor road conditions can lead to vehicle crashes, which can cost billions of dollars annually and cause fatalities. (ASCE 2017; U.S Department of Transportation 2015; TRIP 2019).

Ultra-high performance concrete (UHPC) is being used to solve challenging concrete structural applications where conventional concrete would otherwise deteriorate. UHPC is preferred for its high compressive and tensile strengths, which are achieved by a low water-cementitious materials ratio (*w*/*cm*), optimized particle gradation, and adding materials such as silica fume and steel fibers to the matrix. Steel fibers also increase other mechanical properties, such as splitting tensile (indirect tensile) and flexural (modulus of rupture) strengths.

Quality Assurance and Quality Control (QA/QC) are usually conducted during construction to ensure that the concrete materials meet minimum requirements as required by specification. When a concrete element undergoes QA/QC or a forensic investigation, a partially destructive method is generally used to core cylindrical specimens and saw prismatic specimens from the concrete element to evaluate the compressive and flexural strengths of the concrete in question. Although the in-place flexural strength of a concrete element can be determined by testing sawn prismatic specimens, sawing prismatic specimens causes significant damage to the concrete element and the specimens resulting in unreliable and costly results.

In forensic investigations, it is much easier to extract cylindrical specimens from a

concrete element to test the compressive strength than it is to extract prismatic specimens to test the flexural strength. However, the flexural strength is usually preferred as it is more representative of the real life loading scenario than the compressive strength, especially in pavements, slabs, and bridges. Previous researchers and institutions have determined relationships between the compressive, splitting tensile, and flexural strengths for concrete with different parameters and properties (Raphael 1984; Pul 2008; Xu and Shi 2009; Russell and Graybeal 2013; Ramadass 2014; ACI 2014; Esquinas et al. 2016; Amudhavalli and Poovizhiselvi 2017; Campos et al. 2020). Researchers generally predict the flexural strength or splitting tensile strength based on only the compressive strength resulting in a non-mixture-specific prediction. Furthermore, the previous studies have not considered the steel fiber content as a potential factor for predicting UHPC strengths. The present study uses varying steel fiber contents as well as direct tensile, splitting tensile, compressive and flexural strengths of 60 specimens to develop preliminary empirical models that correlate the direct tensile first crack, post-cracking strengths, and fiber content with the splitting tensile, flexural (modulus of rupture), and compressive strengths at 28 days for non-proprietary UHPC. The accuracy of the developed models is verified by comparing their predictive capabilities with the actual strengths obtained from the laboratory tests.

2 Literature Review

2.1 Ultra-High Performance Concrete

2.1.1 Introduction

There are several factors that affect the strength of concrete: mix proportions, cement type, water-cementitious materials ratio (*w*/*cm*), temperature, mixture uniformity, admixtures, aggregate strength and abrasion characteristics, aggregate shape and size, specimen shape and

size, and air content (Taylor et al. 2019; Ajamu and Ige 2015). Ultra-High Performance Concrete (UHPC) is defined by the United States Federal Highway Administration as being a type of concrete composite that exhibits a compressive strength greater than 21.7 ksi and has a sustained post-cracking tensile strength greater than 0.72 ksi (De La Varga et al. 2018). The FHWA continues to define UHPC as a material consisting of an optimized gradation of granular constituents, water-cement ratio less than 0.25, and a high fiber content (De La Varga et al. 2018). Further, UHPC has a discontinuous pore structure that inhibits liquid ingress resulting in a more durable concrete (De La Varga et al. 2018). The mixture materials used in UHPC include portland cement, fine sand, silica fume, high-range water-reducing admixture, steel fibers, and water (Russell and Graybeal, 2013). UHPC is commonly utilized to resist large stresses when normal or high strength concretes cannot meet the required design strengths. Practicing bridge engineers use UHPC to create strong durable bridge joints for precast and prestressed bridges. Furthermore, the high tensile strength of UHPC allows engineers and architects to design complex columns and frames that are light and durable. UHPC can be more cost-effective than normal or high strength concrete due to the enhanced durability which increases service life and reduces maintenance and rehabilitation of structures that utilize UHPC. UHPC has also been utilized for sustainable designs for the aforementioned reasons (Russell and Graybeal 2013).

2.1.2 Steel Fibers

The steel fibers used in UHPC are generally 0.512 to 1.18 in. long with a diameter of 0.0078 to 0.0216 in. (De La Varga et al. 2018). These fibers are used to increase the strength and performance of the UHPC mixtures. Fibers restrain UHPC which reduces internal damage when exposed to deicing salts and freeze-thaw cycling (Russell and Graybeal, 2013). The fiber reinforcement also increases the tensile strength of UHPC even after cracking due to bridging

action. Bridging action is the ability for UHPC to transfer tensile stresses to the steel fiber reinforcement over a crack. A fiber content of 2%, used in mixtures by suppliers of UHPC, is commonly used for most structural applications in the United States (De La Varga et al. 2018). There are few studies (Wu et al 2015; Hoang and Fehling 2017) that examine other fiber contents and the effect of fiber content on the predictive capabilities of the mechanical properties of UHPC.

2.1.3 Mechanical Properties

Compared to conventional normal strength and high-strength concrete, UHPC has a higher compressive, indirect tensile, direct tensile, and flexural strength (Russell and Graybeal 2013; De La Varga et al. 2018). Typical UHPC has a compressive strength range of 20 to 30 ksi and a tensile cracking range of 0.72 to 1.5 ksi (Russell and Graybeal 2013; De La Varga et al. 2018). Comparatively, normal strength concrete has an average compressive strength of 2.17 to 4.35 ksi and high-strength concrete has a compressive strength greater than 8 ksi. It is important to note that the normal concrete strength classification has not been defined by any code, however, the normal strength classification is common. Furthermore, only the lower bound high-strength limit has been stated by ACI 363 (ACI 2010). UHPC gains its strength from compaction, high cement content, low *w*/*cm*, no coarse aggregate, and steel fibers (Russell and Graybeal 2013; De La Varga et al. 2018). Researchers have also determined that steel fibers significantly affect the direct tensile, indirect tensile, and flexural strengths (De La Varga et al. 2018; Hoang and Fehling 2017).

2.2 Ultra-High Performance Concrete Strength Tests

2.2.1 Compressive Strength

The compressive strength test for UHPC is similar to that of normal and high-strength concretes. ASTM C39 (ASTM 2018a) describes the method and procedure for testing cylindrical concrete specimens in compression. A universal testing machine is used to break cylinders in compression, however, a different load rate of 150 psi/sec is used for UHPC (De La Varga et al. 2018). The complete set of modifications to ASTM C39 is found in ASTM C1856 (ASTM 2017), which describes the procedures for fabricating and testing UHPC specimens.

2.2.2 Splitting Tensile Strength (Indirect Tensile Strength)

The splitting tensile strength test is an indirect tensile test that utilizes the same shape and size specimen as the compression test. ASTM C496 (ASTM 2018b) describes the method and procedure for testing concrete specimens in splitting tension. The universal testing machine is used with a splitting tensile jig assembly to hold the specimen during the test. The splitting tensile test for UHPC is the same as normal and high-strength concretes, however, a load rate of 500 psi/min is used instead of 145 psi/min (De La Varga et al. 2018). The splitting strength is obtained by applying a load along the length of the cylinder until it breaks in indirect tension.

2.2.3 Flexural Strength (Modulus of Rupture)

The flexural strength is determined as described in ASTM C1609 (ASTM 2019) using a flexural testing apparatus and third-point loading, however, the standard is modified for UHPC. The complete set of modifications to ASTM C1609 is found in ASTM C1856 (ASTM 2017), which describes the appropriate steel fiber length and corresponding beam cross-sectional dimensions.

2.2.4 Direct Tensile Strength

The direct tensile test for concrete is a complex procedure that requires more precision than the indirect tension tests described previously. The main issue with testing concrete in tension is the gripping assembly. In order to test UHPC in tension, the gripping assembly must grip the specimen in such a way as to not introduce stress concentrations or bending stresses. If stress concentrations are present during the test, then the concrete specimen will not break in true direct tension. Researchers have designed gripping assemblies to eliminate stress concentrations in the concrete specimens. Graybeal and Baby (2013) developed a gripping assembly that can potentially eliminate these stress concentrations by adhering aluminum plates to rectangular concrete specimens. The aluminum plates are tapered so that the aluminum plates transfer stress uniformly throughout the length of the concrete specimen to ensure that the specimen breaks within the instrumented gauge length. Dog bone shaped concrete specimens have also been considered due to the existence of standardized procedures for similarly shaped metal specimens. However, because dog bone shaped specimens are difficult to extract from structural elements for forensic investigation, the dog bone shape specimen is not recommended for direct tensile testing of UHPC if QA/QC is required (Graybeal and Baby 2013). Another method for determining the direct tensile strength of concrete uses cylindrical specimens. This method adheres the ends of a cylindrical concrete specimen to the testing machine with a high strength adhesive and a uniaxial tensile force is applied to the specimen (Graybeal and Baby 2013). This particular method is desirable due to the elimination of bending stresses within the specimen; however, stress concentrations near the ends of the specimen can develop which prematurely cracks the specimen resulting in a failure that is not true direct tension (Graybeal and Baby 2013). Furthermore, adhering the specimen to the testing machine is a difficult and time

consuming procedure (Graybeal and Baby 2013). It is important to note that the direct tensile test assembly can include hinges to reduce the effects of bending stresses in the specimen, however, this can lead to inaccurate post-cracking strengths due to the relative rotation of the specimen after initial cracking occurs (Russell and Graybeal 2013).

2.3 Relationships between Mechanical Properties of Concrete

2.3.1 Introduction

There is extensive research on correlation models for the mechanical properties of normal strength concrete and high-strength concrete. The mechanical properties that have been correlated by other researchers include the compressive, flexural (modulus of rupture or MOR), indirect tensile (splitting tensile), and direct tensile strengths.

Correlation models are useful to professional engineers and researchers due to their efficiency, ease of use, accuracy and cost reduction. The need for correlation models such as the compressive and flexural strength relationship model can be seen in the QA/QC industry. To obtain the flexural strength of beam specimens for forensic research and QA/QC purposes, segments of a concrete element must be cut out of the concrete structure. Forensic investigations and QA/QC enforcement can be expensive and destructive because cores and prismatic specimens cause damage to the concrete element. Also, areas of the concrete element from where such specimens are collected must be repaired. Consequentially, this operation usually results in the closure of the pavement, building, or bridge in question, which is time consuming and costly (Hammitt 1974). Furthermore, strength testing core and sawed prismatic specimens is more difficult and time consuming than strength testing field prepared cast specimens. A correlation coefficient can be obtained through trial batching to relate the compressive strength and flexural strength of concrete, which is usually done for slabs and pavements allowing for the flexural

strength to be estimated from the compressive strength (Lane 1988). Thus, a model or relationship that could accurately predict the strength throughout a concrete element's life without trial batching or obtaining cores or sawed beams would be ideal for QA/QC purposes as well as for forensic and research investigations.

2.3.2 Relationship between Compressive and Flexural Strengths

The compressive strength is primarily used for QA/QC and the flexural strength is used to determine deflections and cracking stresses for a concrete element. Controlling premature cracks is imperative to the overall health of a concrete structure because cracks degrade concrete and expose steel reinforcement to corrosion inducing factors (Ajamu and Ige 2015). Several factors that affect the compressive strength also affect the flexural strength to a degree. The flexural strength of a fiber reinforced concrete specimen is affected by the quality of fabrication, fiber content, fiber shape and size, fiber material, ambient temperature, mix temperature, relative ambient humidity, curing, and adherence to the testing procedure (Taylor et.al. 2019; De La Varga et al. 2018; Hoang and Fehling 2017).

Researchers have proposed relationships between the compressive strength of concrete cylinders and the flexural strength of concrete beams. The compressive strength of concrete is often said to correlate with the flexural strength. However, the literature points toward the notion that compressive strength and flexural strength do not increase at the same rate (Ahmed et al. 2014). The compressive strength has a nonlinear correlation with the flexural strength of concrete (Campos et al. 2020). The correlation between compressive and flexural strengths can be traced back to a study by Raphael (1984) who developed a power regression model of the following form:

$$f_r = af_c^n \quad \text{(Eq. 2.3.2.1)}$$

where,

$f_r = flexural\ strength$ (modulus of rupture)

$a = regression\ coefficient$

$f_c = compressive\ strength$ and

$n = power\ regression\ coefficient$

The regression coefficients a and n account for the properties of the concrete such as *w*/*cm* and other properties. Regression models relating the compressive and flexural strengths of concrete have been proposed by other researchers. According to Ahmed et al. (2014), the square root relationship used by many design codes is not suiTable for a variety of concrete strength classifications. These researchers found the power model to be more appropriate for a larger range of concrete strength classifications.

2.3.3 Relationship between Indirect Tensile and Compressive Strengths

The indirect tensile strength, or splitting tensile, test is another useful concrete strength parameter. The indirect tensile strength is used as a substitute for the flexural strength because it is much easier to extract and test core specimens in indirect tension than it is to saw, prepare, and test prismatic specimens in flexure. The indirect tensile and compressive strength specimens also fail in a similar way which makes them attractive for correlation modeling. The splitting tensile test is unique because it is loaded in compression but breaks in tension. This is accomplished by loading a cylinder in compression along its length until the cylinder breaks or splits in half due to internal tensile stresses along the diameter of the specimen. Because the splitting tensile and compressive strengths are tested and loaded in a similar way, various researchers have proposed

correlation models, similar to Eq. 2.3.2.1, between the two concrete strengths (Pul 2008; Xu and Shi 2009; Russell and Graybeal 2013; Ramadass 2014; ACI 2014).

$$f_{st} = af_c^n \qquad \text{(Eq. 2.3.3.1)}$$

where,

$f_{st} = splitting$ tensile $strength$ (indirect tensile)

$a = regression\ coefficient$

$f_c = compressive\ strength$ and

$n = power\ regression\ coefficient$

2.3.4 Relationship between Direct Tensile, Flexural, and Compressive Strengths

Conventional concrete is mostly used to resist compressive and bending stresses in an element and concrete tensile strength is usually only considered in terms of first crack. For fiber reinforced concrete the direct tensile test is a difficult and time-consuming procedure but provides a more accurate representation of post-crack behavior than the splitting tensile test (Russell and Graybeal 2013). This strength parameter is rarely used in designing structures or correlating other strength parameters such as the compressive and flexural strengths due to the difficulty of obtaining accurate direct tensile strength data. Consequentially, little information regarding correlation models between the direct tensile and flexural strengths was found during this literature review. Although the direct tensile strength is a less important strength parameter for normal strength and high-strength concretes, it is a more useful strength parameter in structural designs that utilize UHPC, which has a much larger post-cracking tensile capacity than the first crack capacity of conventional concrete. UHPC is designed to resist large compressive, bending, and tensile stresses.

3 Approach and Methods

3.1 Introduction

The approach and methods consists of experimental procedures for constructing, curing, and testing 15 non-proprietary ultra-high performance concrete (UHPC) prismatic specimens of varying fiber contents, development of a direct tensile test assembly that closely matches that used by Graybeal and Baby (2013), examination of existing strength data (splitting tensile and flexural), and correlation model development.

3.2 Ultra-High Performance Concrete

3.2.1 Introduction

The non-proprietary UHPC mix proportions used in this study are the same as the non-proprietary J3-UHPC mixture developed previously at the University of Oklahoma (Looney et al. 2019). The non-proprietary J3-UHPC mixture consists of Type I portland cement, ground-granulated blast furnace slag (slag cement), silica fume, dry masonry sand, water, and high range water reducer (Glenium 7920). Table 3.2.1.1 shows the non-proprietary J3-UHPC mix proportions by weight for fiber percentages of 0, 1, 2, 4, and 6% by volume. The fibers used were 0.5 in. in length. When fiber percentages were changed, the quantities of other constituent materials were adjusted proportionally to maintain a constant volume.

Table 3.2.1. 1 Non-proprietary UHPC mix proportions by weight

Material	% Fibers (by volume)				
	0	1	2	4	6
Type I Cement [lb/yd^3]	1204	1192	1180	1156	1131
Slag [lb/yd^3]	602	596	590	578	566
Silica Fume [lb/yd^3]	201	199	197	193	189
Water [lb/yd^3]	401	397	393	385	377
Fine Masonry Sand [lb/yd^3]	2006	1986	1966	1926	1886
Steel Fibers [lb/yd^3]	0	132	265	529	794
Glenium 7920 [oz./cwt]	18	18	18	23	28
Glenium 7920 [oz/yd^3]	361	358	354	443	528

3.2.2 Non-Proprietary J3-UHPC Mix Procedure

A total of five batches were mixed to cast the final 15 test specimens. The volume of UHPC mixed for each fiber percentage batch was 0.193 ft^3 and each batch was mixed using a high shear Blakeslee planetary mixer. Due to the low *w*/*cm*, fine particles, high range water reducer (HRWR), and steel fibers, a very specific mix procedure is required to successfully mix the dry materials, water, HRWR, and steel fibers. The mixing procedure used for the non-proprietary J3-UHPC is as follows:

1. The dry materials (Type I cement, masonry sand, silica fume, and slag) were added to the mixing bowl.
2. The mixing bowl was inserted into the mixer and the mixing bowl was raised into position.
3. The mixer was turned on and the dry materials were allowed to mix for 10 minutes. See Figure 3.2.2.1.

Figure 3.2.2. 1 Mixing of dry J3-UHPC materials

4. While the dry materials were mixing, half of the high range water reducer was added to the mixture water shown in Figure 3.2.2.2.

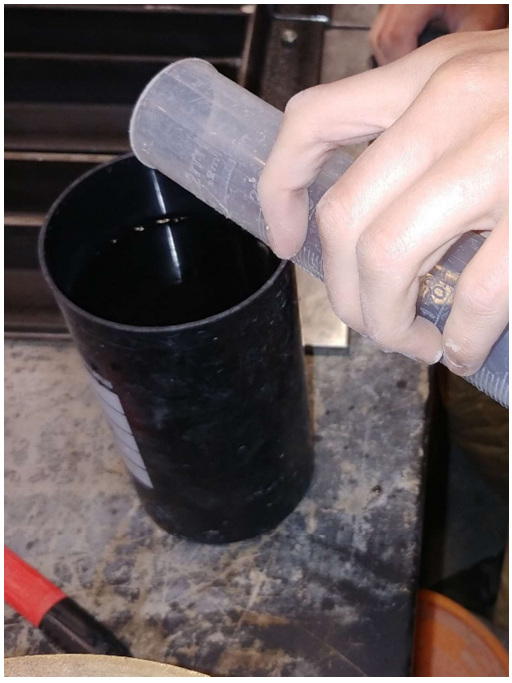

Figure 3.2.2. 2 Adding half of the HRWR to the mixture water

5. After mixing the dry materials, the water was slowly poured into the mixing bowl over a course of 2 minutes shown in Figure 3.2.2.3.

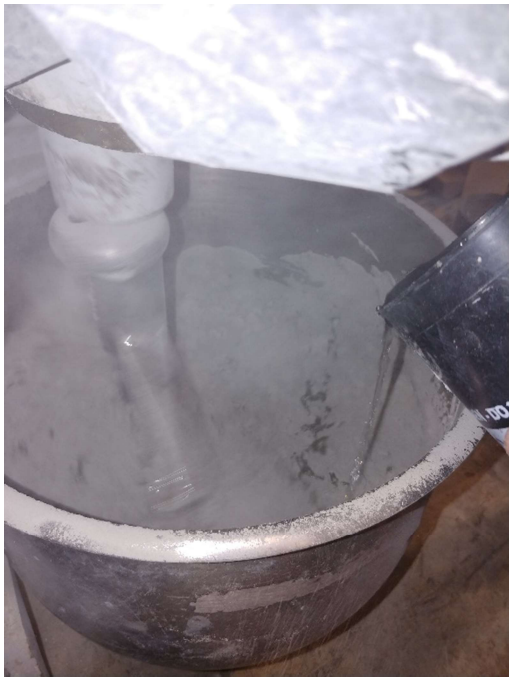

Figure 3.2.2. 3 Adding mixture water to mixing bowl

6. The materials were allowed to mix for 1 minute.
7. The remaining high range water reducer was poured into the mixing bowl over the course of 1 minute as shown in Figure 3.2.2.4.
8. The materials were allowed to mix for 10 minutes or until the consistency of the materials transformed into a fluid mass. If the mixture did not transform, one ounce per hundred pounds of cement weight of high range water reducer was added to the mix until transformation was achieved. This transformation is shown in Figure 3.2.2.5.

Figure 3.2.2. 4 Adding remaining HRWR to mixing bowl

(a) (b) (c)

Figure 3.2.2. 5 J3-UHPC mixing stages: (a) mixture after HRWR, (b) 5 minutes after HRWR, (c) 10 minutes after HRWR

9. For batches that included steel fibers, the fibers were slowly poured into the mixing bowl and allowed to mix for 2 minutes after the materials had transformed into a fluid mass as shown in Figure 3.2.2.6.

(a) (b) (c)

Figure 3.2.2. 6 J3-UHPC mixing stages: (a) adding steel fibers, (b) after 2 minute, (c) finished UHPC mix

Once the mixing procedure was complete, a flow test was performed and then the specimen molds were filled. The same procedure was conducted for fiber percentages of 0, 1, 2, 4, and 6% by volume. The prism molds, HRWR, and steel fibers used in this study can be seen in Figure 3.2.2.7.

(a) (b) (c)

Figure 3.2.2. 7 (a) UHPC prismatic molds (b) HRWR, (c) steel fibers

3.2.3 Flow Test

A flow test was performed as per ASTM C1437 and ASTM C1856 after the mixture had achieved a fluid state. The procedure for the flow test of the non-proprietary J3-UHPC is as follows:

1. The flow table was cleaned and lightly moistened before each flow test.
2. In a fluid state, a small portion of the mixture was poured into the mold to fill in a single layer. The filled mold is shown in Figure 3.2.3.1.
3. The J3-UHPC was not tamped nor was the flow table dropped at any point during the flow test.
4. The flow table and outside of the mold were cleaned with a damp rag.
5. A timer was set for 2 minutes.

Figure 3.2.3. 1 Flow table, mold, and UHPC

6. The timer was started as the mold was lifted from the flow table.
7. After the J3-UHPC was allowed to flow for 2 minutes, (see Figure 3.2.3.2) the maximum and minimum diameters of the J3-UHPC mass were measured.
8. The average of the two diameters was taken as the flow.

If a flow between 8 in. and 10 in. was not achieved, then additional HRWR, in increments of one ounce per hundred pounds of cement weight, would be added to the remaining material in the mixing bowl to increase the flow. The UHPC would be allowed to mix for another 2 minutes and the flow test would be repeated. Once the proper flow was achieved, the UHPC was poured into three prismatic molds and three 3 inch by 6 inch cylinders. The filled prismatic molds are shown in Figure 3.2.3.3.

Figure 3.2.3. 2 UHPC mass flow after 2 minutes

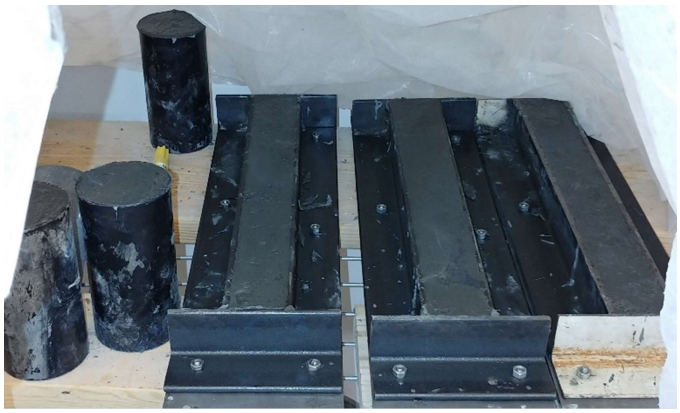

Figure 3.2.3. 3 Cylinder and prismatic molds filled with J3-UHPC

3.2.4 Direct Tensile Molds

Prismatic molds were fabricated specifically for the direct tensile specimens. The prismatic mold was designed to make a 2 in. by 2 in. by 17 in. UHPC prism. Each prismatic mold consists of one large steel base plate, four 90 degree steel angles, and 8 bolts. The steel base plate is 6 in. by 21 in. by 0.375 in. thick. Two of the four 90 degree steel angles are 6 in. by

2 in. by 2 in. and the other two 90 degree steel angles are 17 in. by 2 in. by 2 in.. The 17 in. steel angles were welded to the 6 in. steel angles at 90 degrees to create a prismatic mold as shown in Figure 3.2.4.1. The mold is then assembled by fastening the steel angles to the steel plate with bolts to prevent the mold from sliding or rotating. Due to the high flowability of UHPC, a sealant was used to close any gaps in the mold to prevent the mold from leaking UHPC. A thin layer of oil-based form release was applied to the mold before specimen casting to prevent the UHPC from sticking to the mold. Three prismatic molds were fabricated for this study. The prismatic molds were cleaned and lightly polished before each use. In total, the three prismatic molds were used to construct 15 prismatic specimens.

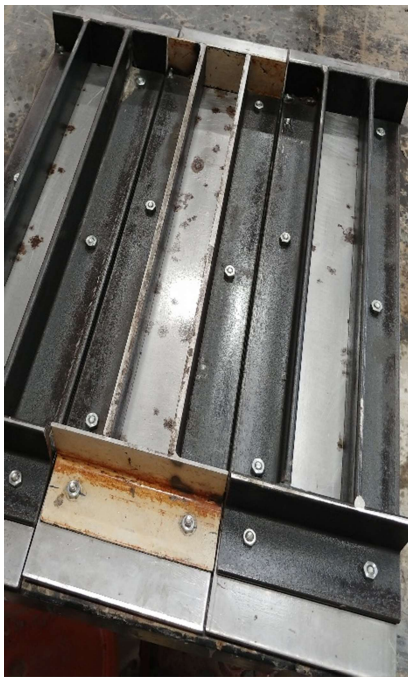

Figure 3.2.4. 1 Direct tensile test specimen molds

3.2.5 Heat Curing

The freshly mixed UHPC specimens were allowed to cure in their molds under a standard laboratory environment of 73 °F and 50% relative humidity for 24 hours (see Figure 3.2.5.1). After 24 hours the prismatic and cylindrical UHPC specimens were demolded and placed in an environmentally controlled chamber. The specimens were allowed to cure in the environmental chamber at 194° F and 95% relative humidity for 48 hours as per ASTM C1856. All of the direct tensile prismatic specimens and their corresponding cylinders were heat cured for this study.

Figure 3.2.5. 1 Specimens in standard laboratory environment

3.3 Existing UHPC Strength Data

In total, results from 30 non-proprietary UHPC specimens tested at OU were used in this study. A portion of these specimens were tested under splitting tension and another portion under flexure. The splitting tensile strength and flexural strength data was taken from Dyachkova (2020). The existing data of the strength parameters and the steel fiber contents were used to develop a matrix for statistical analysis.

A total of 15 cylindrical specimens, each having a diameter of 3 in. and a length of 6 in. were prepared and tested under indirect splitting tension as per ASTM C496 (ASTM 2018b) using a universal testing machine at 28 days and a modified load rate of 500 psi/min (Dyachkova 2020).

The flexural strength or modulus of rupture was obtained by testing 15 prismatic specimens, each having a 3 in. x 3 in. and 12 in. length, in flexure as per ASTM C1856 and ASTM C1609 (ASTM 2017: ASTM 2019) using a flexural testing apparatus and third-point loading at 28 days (Dyachkova 2020).

Averages were determined from the strength parameters to obtain the average splitting tensile and flexural strengths for each steel fiber content percentage. The mechanical properties and their corresponding steel fiber contents obtained from previous research are shown in Table 3.3.1. The matrix and Figure 3.3.1 shows that possible correlations may exist between the flexural and splitting tensile strengths of J3-UHPC. Compared to 4% steel fiber content, a decrease in strength is observed at a steel fiber content of 6% for both flexural and splitting tensile strengths as shown in Figure 3.3.1.

Table 3.3. 1 Existing mechanical property data for J3-UHPC and steel fiber content

Steel Fiber Content (%)	Flexural Stress (psi)	Splitting Tensile Stress (psi)
0	1264	1127
	1244	1432
	1290	997
average	**1266**	**1180**
1	1782	1810
	1713	1985
	1806	2183
average	**1767**	**1990**
2	2468	2457
	2388	2873
	2501	2404
average	**2452**	**2580**
4	3750	3336
	5168	2974
	3924	2947
average	**4281**	**3090**
6	4113	2823
	4680	2964
	2574	2990
average	**3789**	**2930**

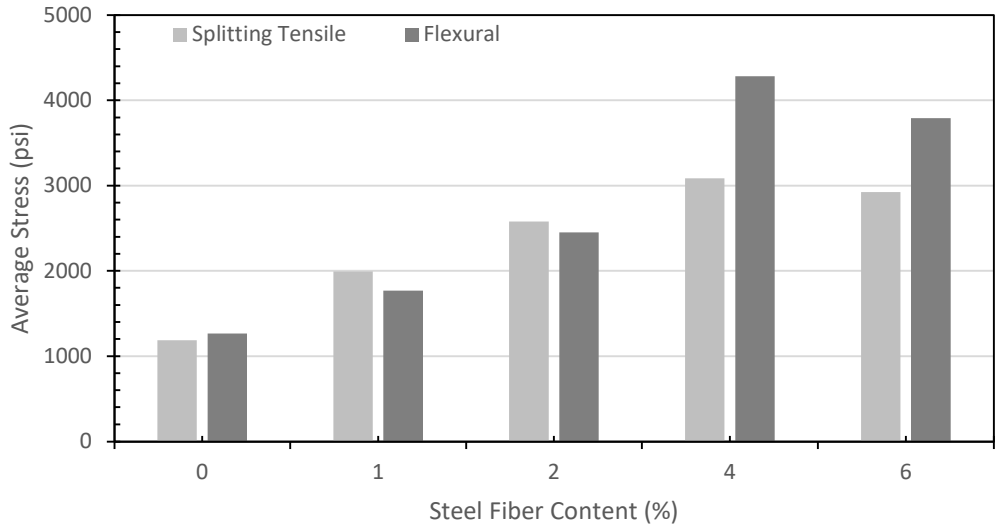

Figure 3.3. 1 Comparison of existing mechanical properties of J3-UHPC and steel fiber content

3.4 Direct Tensile Test Development

3.4.1 Introduction

The direct tensile test assembly - a variation of a testing apparatus designed by Graybeal and Baby (2013) - was fabricated specifically for this study to avoid stress concentration in the test specimen while also being compatible with the available universal testing machine and remaining relatively simple to set up and operate. The assembly was constructed out of steel and aluminum components. Four aluminum plates were adhered to each specimen, two plates on each end of the specimen, and the aluminum plates were connected to a steel frame that connected each end of the specimen to the universal testing machine. The components were fastened with structural bolts. Figure 3.4.1.1 shows a picture of the assembly.

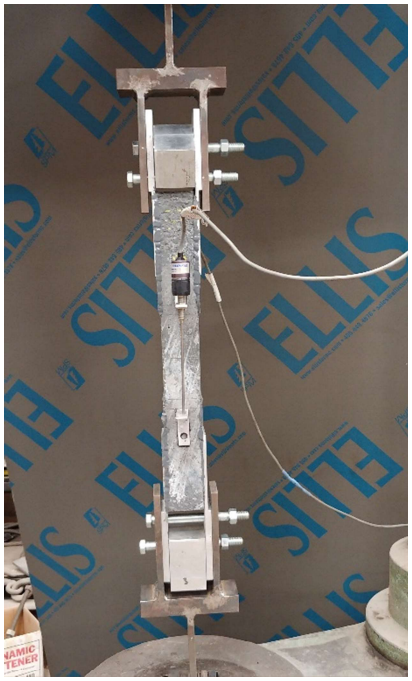

Figure 3.4.1. 1 Direct tensile UHPC test assembly

3.4.2 Aluminum Plate

Two iterations of the aluminum plates were used in this study. The difference between the first and the second iteration is in the design of the ends of the plates. The first iteration of the aluminum plate has a flat end that is 0.040 in. thick, however, a second iteration of the aluminum plate was designed to better transfer the uniaxial tensile stress from the steel frame to the UHPC specimen without producing stress concentrations by linearly tapering the end of the aluminum plate. The aluminum plate design, a modified version of Greybeal and Baby's (2013) design, is 2 in. wide, 10.25 in. in length with thicknesses varying from 0.375 in. at one end to 0.040 in. at the other end. The aluminum plate also includes 2 holes for structural bolts in the 0.375 in. thick section. The stock aluminum plate used to fabricate the fixtures had a length of 10.25 in., a width of 2 in. and a thickness of 0.375 in. Grade 6061 aluminum was chosen due to its high tensile strength, availability, and low cost. A computer numerical control machine (CNC) was used to mill and drill the aluminum stock to design specifications. A four flute, titanium carbonitride (TiCN) coated, 0.5 in. diameter, cobalt steel square end mill was used to mill the aluminum plate and the holes were drilled with a 0.5625 in. diameter carbide-tipped drill bit. In total, 48 plates with tapered ends and 12 plates with flat ends were fabricated for this study. Completed aluminum plates are shown in Figures 3.4.2.1 and 3.4.2.2.

Figure 3.4.2. 1 Aluminum plate with tapered end

Figure 3.4.2. 2 Measurement of four aluminum plates with tapered ends

3.4.3 Steel Frame

A steel frame was fabricated to transfer the uniaxial tensile stress from the testing machine to the aluminum plates. The steel frame was designed to resist the full tensile stress and bending stresses caused by the expected specimen failure loads, and to also act as a hinge in order to self-align and reduce bending stresses in the UHPC specimen. The steel frame consists of two 6 in. by 2 in. by 0.375 in. plates, one 6.25 in. by 2 in. by 0.375 in. plate, and one 5.5 in. by 2 in. by 1 in. plate. Two holes were drilled into the two 6 inch long plates with a 0.5625 inch drill bit. These were intended to line up with the aluminum plates attached to each concrete specimen. The four plates were welded together to create one steel frame. In total, two frames were fabricated for this study. The completed frames are shown in Figure 3.4.3.1.

Figure 3.4.3. 1 Steel frames used to connect specimen to universal testing machine

3.4.4 UHPC Prismatic Specimen and Aluminum Plate Bond

J-B Weld, a high strength two-part epoxy, was used to bond the aluminum plates to the prismatic UHPC specimens. To avoid the possibility of the epoxy debonding under tensile stress, both the aluminum and UHPC contact surfaces were lightly sand blasted. The sand blaster and sand blasting process are shown in Figure 3.4.4.1. The sand blaster and air compressor were set

to 120 psi and the distance between the nozzle and the surface was greater than 2 in. Careful attention and handling of the sand blasting gun was necessary in order to not damage the UHPC or aluminum surfaces. If the nozzle were to be too close to the surface of the UHPC, then the sand blaster could severely damage the specimen. Furthermore, special attention was given to the thin portion of the aluminum plate by extending the distance from the nozzle to the surface to greater than 4 in. to avoid deformation of the plates. Aluminum plates after sand blasting are shown in Figure 3.4.4.2.

(a) (b) (c)

Figure 3.4.4. 1 (a) Sand blaster, (b) aluminum plate sand blasting, (c) aluminum plate sand blasted surface

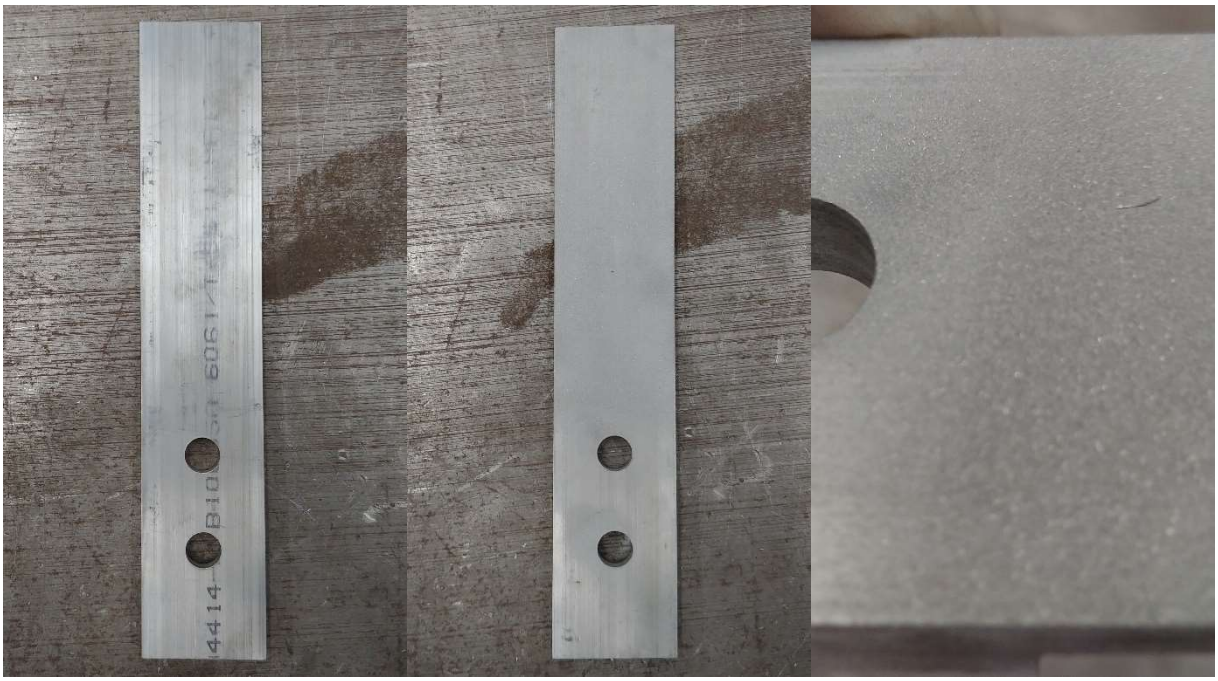

(a) (b) (c)

Figure 3.4.4. 2 (a) Aluminum plate before sand blasting, (b) aluminum plate sand blasted surface, (c) aluminum plate sand blasted surface close up

The two surfaces of the UHPC prismatic specimen that were sand blasted were the surfaces perpendicular to the top exposed surface during casting. Specimen surfaces were prepared from the ends of the specimen to the point corresponding to the end of the aluminum plate. A black line was placed 6.25 in. from both ends of the specimen on the two surfaces perpendicular to the exposed surface in order to identify the sand blasting zone. A prismatic specimen before and after sand blasting is shown in Figure 3.4.4.3

(a) (b) (c)

Figure 3.4.4. 3 (a) UHPC prismatic specimen, (b) UHPC prismatic specimen sand blasted surface halfway, (c) UHPC prismatic specimen sand blasted surface complete

Before the two-part epoxy was applied to the aluminum plates and UHPC prismatic specimen's sand blasted surfaces, the plates were cleaned with acetone to remove any oil or other residue from the CNC milling process. The UHPC prismatic specimen was placed on a level surface with the exposed surface (exposed casting surface) facing up. The 1:1 two-part epoxy's weight was measured to a total of 46 grams (23 grams/epoxy component) per specimen. The epoxy was mixed thoroughly for 2 minutes or until the mixture turned dark grey (see Figure 3.4.4.4). A heavy coat of epoxy was placed on the UHPC specimen's sand blasted surfaces and then the remaining epoxy was placed on the aluminum plates. After all sand blasted surfaces had been coated with epoxy, the aluminum plates were placed onto the UHPC specimen (see Figure 3.4.4.5). The level surface and four 0.5625 in. diameter steel dowels were used to align the

aluminum plates with the UHPC specimen. The steel dowels were inserted into the aluminum plate's 0.5625 in. drilled holes to align and lock the rotation of the aluminum plates on both sides of the UHPC specimen. Four woodworking clamps were used to hold the aluminum plates to the UHPC specimen (see Figure 3.4.4.5) and eight 2 in. by 2 in. by 0.188 in. aluminum plates, four of which had a 0.040 inch linearly tapered edge, were used to distribute the clamping force to the epoxied aluminum plates. A 4.5 in. spacer was used to insure a space of 4.5 in. between the aluminum plates. Figure 3.4.4.6 shows the dowels and spacers used to align the aluminum plates. The clamps were removed after 24 hours when the epoxy had completely cured.

(a) (b) (c)

Figure 3.4.4. 4 (a) Epoxy components, (b) mixed epoxy, (c) specimen and aluminum plates clean and ready for epoxy

(a) (b) (c)

Figure 3.4.4. 5 (a) Epoxy on specimen, (b) epoxy on aluminum plate, (c) specimen and aluminum plates clamped

(a) (b) (c)

Figure 3.4.4. 6 (a) Aluminum plates used to distribute clamping force, (b) steel dowels, (c) 4.5 in. spacer

3.4.5 Direct Tensile Assembly

The complete direct tensile assembly includes the two aluminum blocks, four aluminum plates epoxied to the UHPC prismatic specimen and two steel frames fastened to the aluminum plates with structural bolts. The 2 in. by 2 in. by 3 in. aluminum blocks are used to restrict movement in the aluminum plates (see Figure 3.4.5.2). A quick setting adhesive was applied to the UHPC specimen's surfaces perpendicular to the aluminum plates to bond L-shaped 2 in. by 2 in. by 0.5 in. aluminum gripping tabs (Figure 3.4.5.2) for the linear voltage differential transformers (LVDT).The LVDTs were used to measure deformation during the tension test and determine the average strain over the gage length. The space between the L-shaped tabs was approximately 5.5 in. and were placed 2.25 in. from the center of the specimen within the bounds of the aluminum plates. This length was chosen in order to capture the full tensile response within the instrumental gauge length. A completed direct tension test specimen before placement of the L-shaped tabs is shown in Figure 3.4.5.2.

(a) (b) (c)

Figure 3.4.5. 1 (a) L-shaped tabs, (b) structural bolts, (c) aluminum block

Figure 3.4.5. 2 Direct tensile assembly before adding the L-shape tabs

3.5 Direct Tensile Test

3.5.1 Introduction

The direct tensile strength was obtained by testing 15 prismatic specimens, each having a 2 in. by 2 in. cross-section and 17 in. length, in direct tension as per Graybeal and Baby (2013) using a modified direct tensile testing apparatus. A total of 15 corresponding cylindrical specimens, each having a diameter of 3 in. and a length of 6 in. were prepared and tested under uniaxial compressive loading as per ASTM C1856 (ASTM 2017) methods using a compression testing machine. The steel fiber contents tested are 0%, 1%, 2%, 4%, and 6%. Figure 3.5.1.1 shows complete sets of specimens ready for testing.

Figure 3.5.1. 1 Complete sets of specimens

3.5.2 Setup and Testing Procedure

Each specimen was carefully placed in the universal testing machine and fastened with structural bolts as shown in Figure 3.5.2.1. LVDTs were placed in the two aluminum L-shaped gripping tabs. The same LVDT configuration was used for all of the specimens. After securing the LVDTs, the specimen was aligned with the steel frames by using a level. In order to eliminate stress concentrations or bending stresses and to ensure concentric loading, hinges were used at the top and bottom of the testing assembly. Furthermore, a neoprene pad and a rod was used to create a swivel at the bottom connection to allow the tensile assembly to self-align with the tensile load. Once the specimen was vertical, the initial LVDT displacements were measured and recorded. It is important to note that the LVDT gripping tabs were placed within the bounds of the aluminum plates. The specimens were loaded at a rate between 100 lb/sec to 150 lb/sec until the LVDTs reached their maximum extension or until the specimen failed. Load and LVDT deflection were measured throughout the test and recorded using a single data acquisition system. The average strain over the gauge length was then calculated from the LVDT deflections by using Eq. 3.5.2.1.

$$\varepsilon = \frac{\Delta L}{L} \qquad \text{(Eq. 3.5.2.1)}$$

where,

$\varepsilon = strain$,

$\Delta L = change\ in\ length\ of\ LVDT$, and

$L = original\ length\ of\ LVDT$

The direct tensile post-cracking stress was determined by locating the maximum tensile force from the stress-strain curve and then using Eq. 3.5.2.2.

$$\sigma_{pc} = \frac{F_{pc}}{A} \qquad \text{(Eq. 3.5.2.2)}$$

where,

$\sigma_{pc} = post\ cracking\ (maximum\ tensile)\ stress\ (psi)$,

$F_{pc} = post\ cracking\ (maximum\ tensile) force\ \ (lb)$, and

$A = cross\text{-}sectional\ area\ (in.2)$

The direct tensile first crack stress was determined by locating the first crack from the stress-strain curve and then using Eq. 3.5.2.3.

$$\sigma_{fc} = \frac{F_{fc}}{A} \qquad \text{(Eq. 3.5.2.3)}$$

where,

$\sigma_{fc} = stress\ at\ first\ crack\ (psi)$,

$F_{fc} = tensile\ force\ at\ first\ crack\ (lb)$, and

$A = cross\text{-}sectional\ area\ (in.2)$

The tensile modulus of elasticity (MOEt) was calculated by using Eq. 3.5.2.4.

$$E_t = \frac{\sigma_{fc}}{\varepsilon_{fc}} \qquad \text{(Eq. 3.5.2.3)}$$

where,

$E_t = tensile\ modulus\ of\ elasticity\ (MOEt)\ (psi)$,

$\sigma_{fc} = stress\ at\ first\ crack\ (psi)$, and

$\varepsilon_{fc} = strain\ at\ first\ crack$

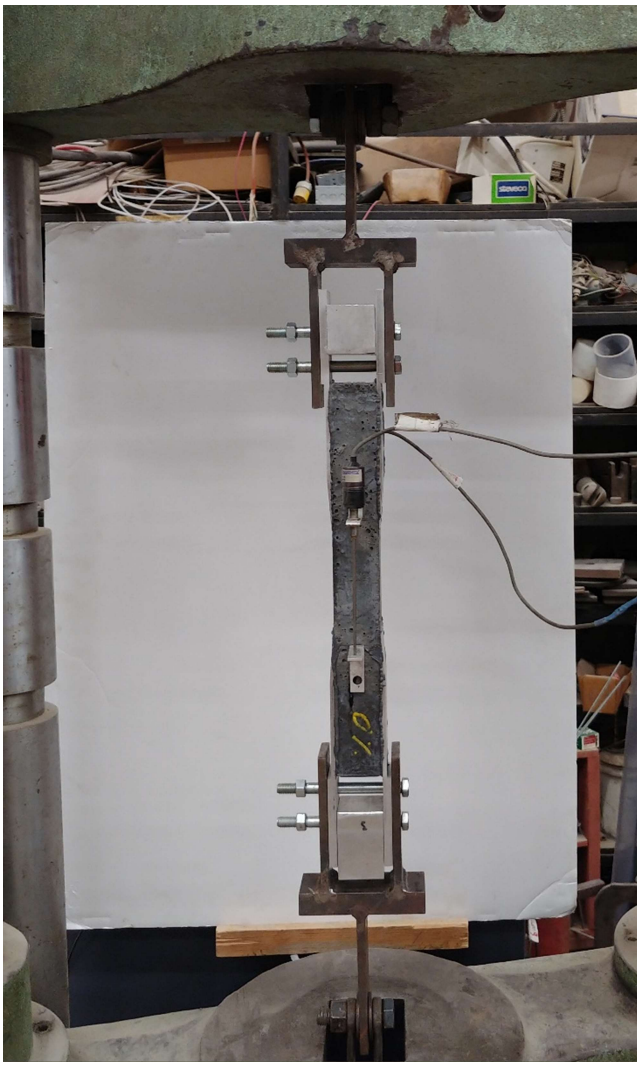

Figure 3.5.2. 1 Direct tensile specimen in the universal testing machine

3.6 Model Development

Statistical regression software was used to analyze the steel fiber contents and the strength parameters from the concrete cylinders and beams to determine empirical relationships between the compressive, splitting tensile, flexural, and direct tensile strengths at 28 days for UHPC. A significance test was performed on the steel fiber contents and strength parameters using the same statistical software to determine which variables were incorporated into the models.

The steel fiber content and the strength parameters were related with the power, square root, and multi-nonlinear regression models. The root mean square error (RMSE) was used to determine the error in the prediction equations by analyzing the differences in the RMSE of each equation to determine the most accurate model. The RMSE analysis was performed for each regression model with varying fiber contents to better understand the effects of steel fiber content on the regression models.

3.7 ROCA Engineering, Inc. and Oklahoma Center for the Advancement of Science and Technology (OCAST) Joint Project

This project is concerned with the relationship between the compressive and flexural strengths of normal strength concrete and the relationship between the splitting tensile and compressive strengths of high strength concrete. These models are used to predict the flexural strength of normal strength concrete by only utilizing the compressive strength of concrete or to predict the splitting tensile strength of high strength concrete by only utilizing the compressive strength. Overall, the goal of this project is to provide technical advancements to Oklahoma's pavement research efforts as well as to supplement the current study.

The concrete strengths obtained through ROCA Engineering, Inc. amount to 1,482 specimens. Of these, 1,342 specimens are normal strength and 140 specimens are high-strength concrete. For the normal strength specimens, 1,009 were cylindrical specimens and 333 were prismatic specimens. For the high-strength specimens, 70 cylindrical specimens were tested in splitting tension and the remaining 70 cylindrical specimens were tested in compression. The findings of the research concerned with the relationship between the compressive and flexural strengths of normal strength concrete have been published and were used to supplement the current study (Campos et al. 2020).

Normal, high-strength, and ultra-high performance concrete regression models were compared to determine the potential similarities between the three strength classifications. The mechanical properties that were analyzed are compressive, flexural, and splitting tensile strengths. Specifically, the correlation between the compressive and flexural strengths, and the correlation between the splitting tensile and compressive strengths were investigated.

4 Results and Discussion

4.1 J3 Non-Proprietary Ultra-High Performance Concrete

4.1.1 Flow Test and Compressive Test

The mortar flow and compressive cylinder results can be seen in Table 4.1.1.1. Additional high range water reducer beyond the baseline mix was required to attain an acceptable flow for all steel fiber contents. This is most likely due to variations in the composition of the dry materials. The 6% steel fiber content was unable to attain a flow greater than 8 in. even with additional high range water reducer. The 6% steel fiber content mix bled more water with increasing high range water reducer resulting in the clumping of steel fibers. Consequently, the poor distribution of steel fibers could be the leading cause of premature failure commonly seen in 6% steel fiber content tension tests. Comparatively, the 4% steel fiber content mix flowed uniformly, and the fiber distribution was visibly adequate. Additional high range water reducer was required for the 4% steel fiber content mix, however, unlike 6% steel fiber content, 4% steel fiber content was able to attain a flow greater than 8 in.

From Table 4.1.1.1 the compressive strength generally increases as the steel fiber content increases. The flowability and poor fiber distribution seen in the 6% steel fiber content mix seems to not have a negative effect on the compressive strength. It is important to note that the excess bleed water that accumulates at the top of the 6% steel fiber content cylinders could negatively affect the compressive strength. This negative effect was not observed, likely due to the top and bottom surfaces of all the cylinders in this study being ground down and this poor portion of content removed.

Table 4.1.1. 1 Flow test and compressive test results

Steel Fiber Content (%)	Specimen	Compressive Strength (psi)	Flow (in.)	Glenium 7920 (oz./cwt)
0	1	18366	10.00	23
	2	16356		
	3	20492		
	average	**18400**		
1	1	18049	-	23
	2	18071		
	3	17619		
	average	**17910**		
2	1	20881	8.00	23
	2	18940		
	3	20497		
	average	**20110**		
4	1	20632	9.25	26
	2	21069		
	3	21104		
	average	**20930**		
6	1	24014	6.00	27
	2	23132		
	3	24823		
	average	**23990**		

Note: Glenium 7920 = High Range Water Reducer

4.2 Direct Tensile Test

4.2.1 Introduction

The post-cracking stress, first crack stress, strains, and modulus of elasticity results from the direct tensile test can be seen in Table 4.2.1.1. Table 4.2.1.1 shows that on average the direct tensile first crack strength for steel fiber contents of 0%, 1%, 2%, 4%, and 6% is 1,043 psi. Although the first crack strengths have a small nonlinear range, the first crack strains have a negative linear trend with increasing steel fiber content. This observation suggests that the first cracking stress will generally be the same with increasing steel fiber content and the first crack strain will decrease with increasing fiber content. The post-cracking stress has a nonlinear trend

with increasing steel fiber content, however, unlike the first crack strain, the post cracking strain is nonlinear and has no observable correlation with any other mechanical property.

Table 4.2.1. 1 Direct tensile test results

Steel Fiber Content (%)	Specimen	First Crack Stress (psi)	First Crack Strain (με)	Post Cracking Stress (psi)	Post Crack Strain (με)	MOEt (ksi)
0	1	761	-	-	-	-
	2	1017	-	-	-	-
	3	1012	216	-	-	4690
	average	**930**	**216**	**-**	**-**	**4690**
1	1	984	191	984	191	5156
	2	1059	255	1059	255	4153
	3	1017	199	1017	199	5104
	average	**1020**	**215**	**1020**	**215**	**4743**
2	1	1001	189	1210	1231	5299
	2	1135	207	1135	207	5488
	3	1204	188	1225	1000	6393
	average	**1113**	**195**	**1190**	**812**	**5719**
4	1	1022	209	1437	1181	4893
	2	1223	122	1705	3361	10021
	3	1033	124	1638	1800	8353
	average	**1093**	**151**	**1593**	**2114**	**7211**
6	1	958	5.21	1457	99	-
	2	1007	129	1598	481	7821
	3	906	135	1367	1340	6705
	average	**957**	**90**	**1474**	**640**	**7263**

Note: MOEt = Tensile Modulus of Elasticity

A comparison of the direct tensile stresses and the existing maximum flexural and splitting tensile stresses is shown in Figure 4.2.1.1. From Figure 4.2.1.1 a nonlinear trend is observed between the flexural, splitting tensile, direct tensile post-cracking, and the direct tensile first crack stresses. Furthermore, the direct tensile stresses exhibit the same negative trend as the indirect splitting tensile and flexural stresses at 6% steel fiber content. Comparatively, this negative trend is not observed in the compressive stress and is therefore considered a trait of tensile UHPC behavior. Figure 4.2.1.1 also shows that while the tensile stresses have a nonlinear

trend with increasing steel fiber content, the compressive stress generally increases linearly. These trends further strengthen the reliability and practicality of utilizing nonlinear multivariable regression models to accurately predict the mechanical properties of J3-UHPC.

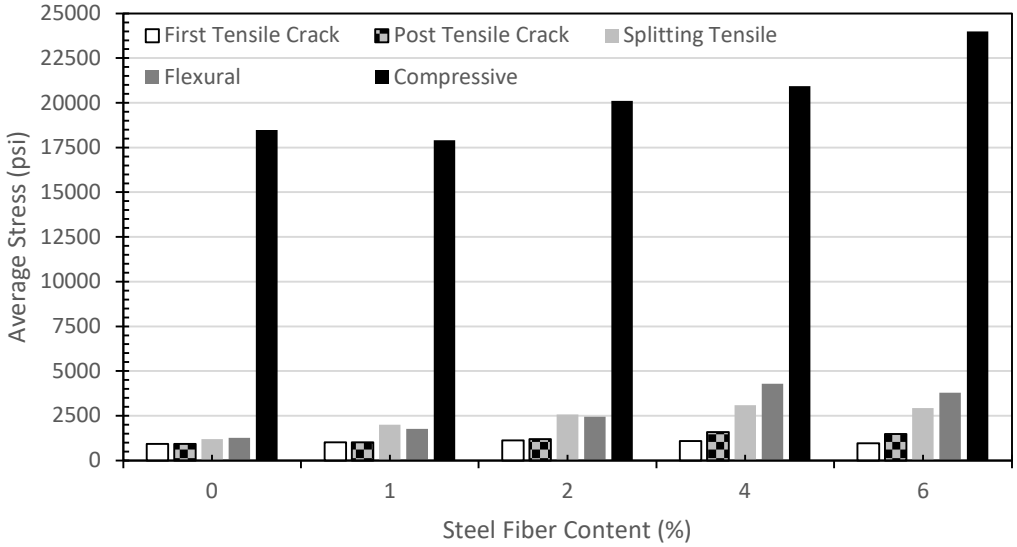

(a)

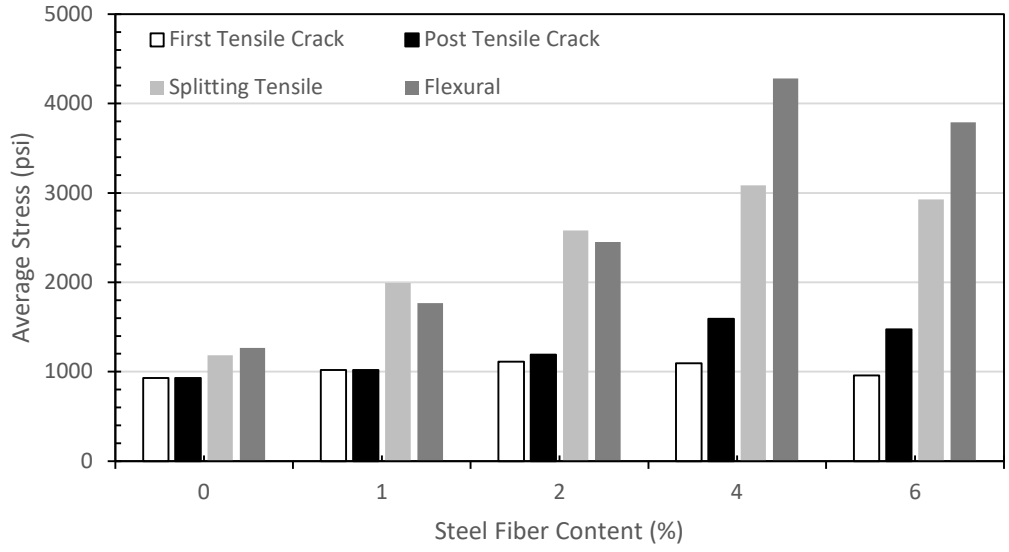

(b)

Figure 4.2.1. 1 Comparison of average J3-UHPC stresses by steel fiber content: (a) comparison of compressive and tensile stresses, (b) comparison of tensile stresses

4.2.2 Direct Tensile Cracking Patterns

Figures 4.2.2.1, 4.2.2.2, and 4.2.2.3 show the cracking pattern that developed throughout the direct tensile test for the 0% steel fiber specimens. All of the specimens cracked within the LVDT instrumented gauge length which allowed for the direct tensile stress-average strain curve to be fully captured. In each case, the crack developed uniformly throughout the specimen. From Figures 4.2.2.1 and 4.2.2.3, it is shown that the crack for specimens 1 and 3 formed near the aluminum plates. Figure 4.2.2.2 shows that the crack or specimen 2 formed near the middle of the specimen. It is unclear if the cracks that developed near the aluminum plates are due to stress concentrations or UHPC material variation. The crack location did not have a negative effect on the tensile strength.

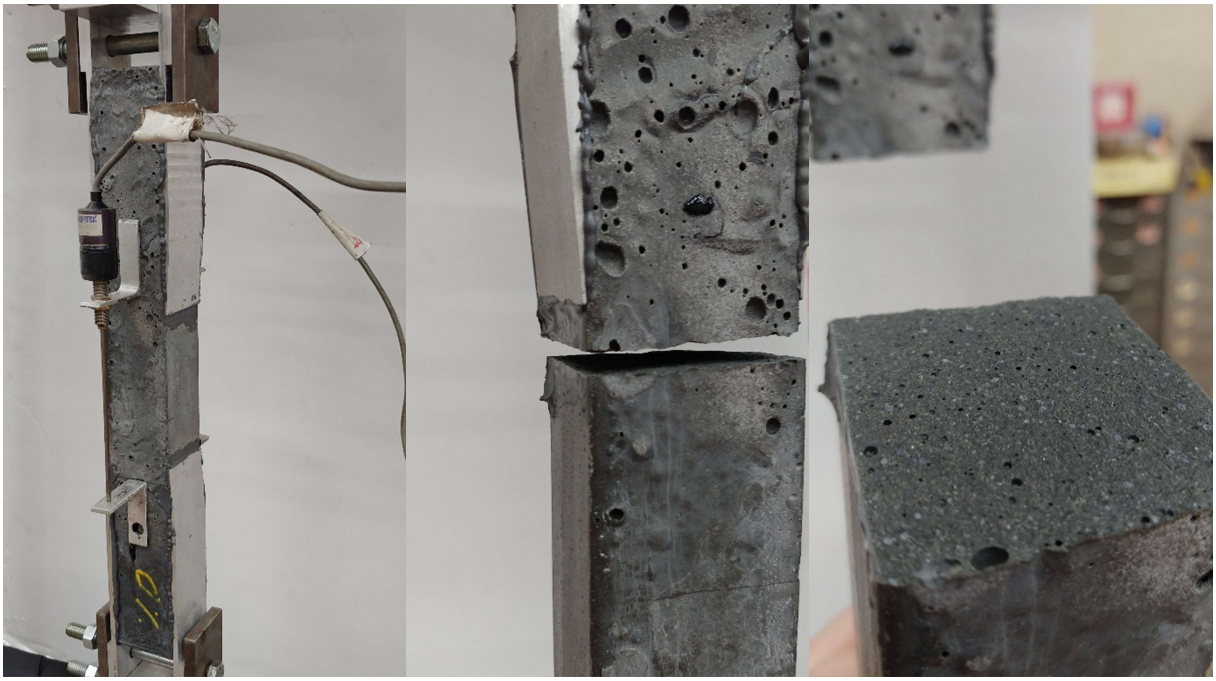

Figure 4.2.2. 1 Crack pattern 0% steel fiber content Specimen 1

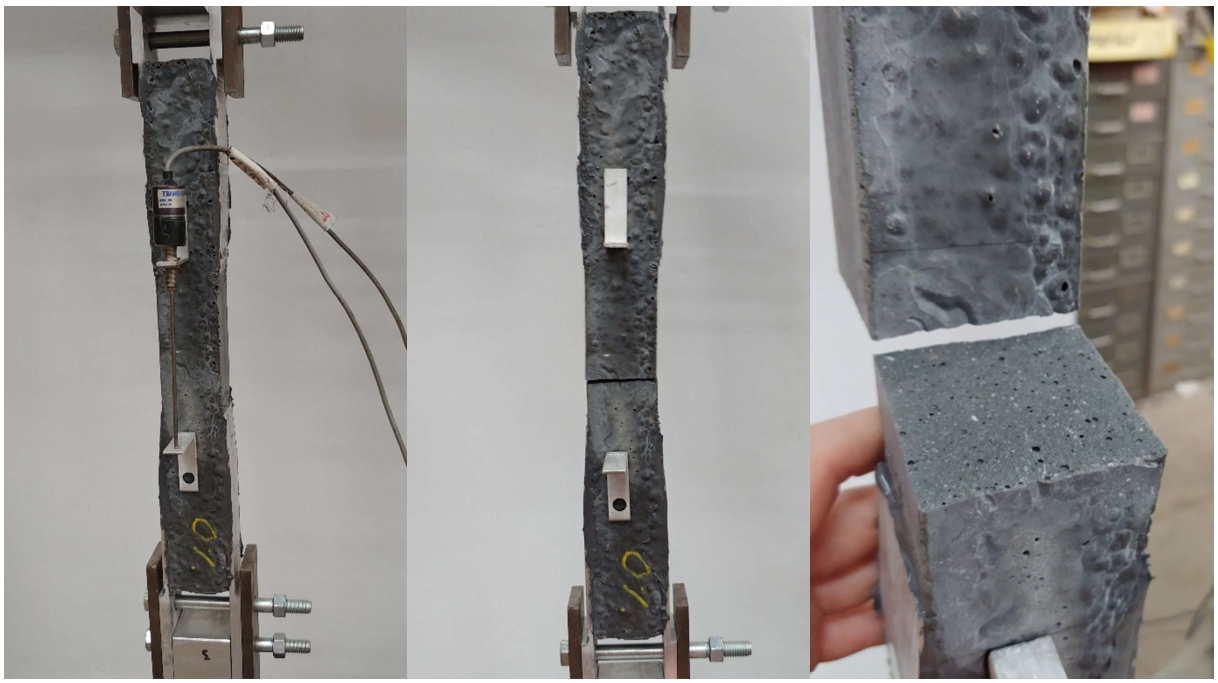

Figure 4.2.2. 2 Crack pattern 0% steel fiber content Specimen 2

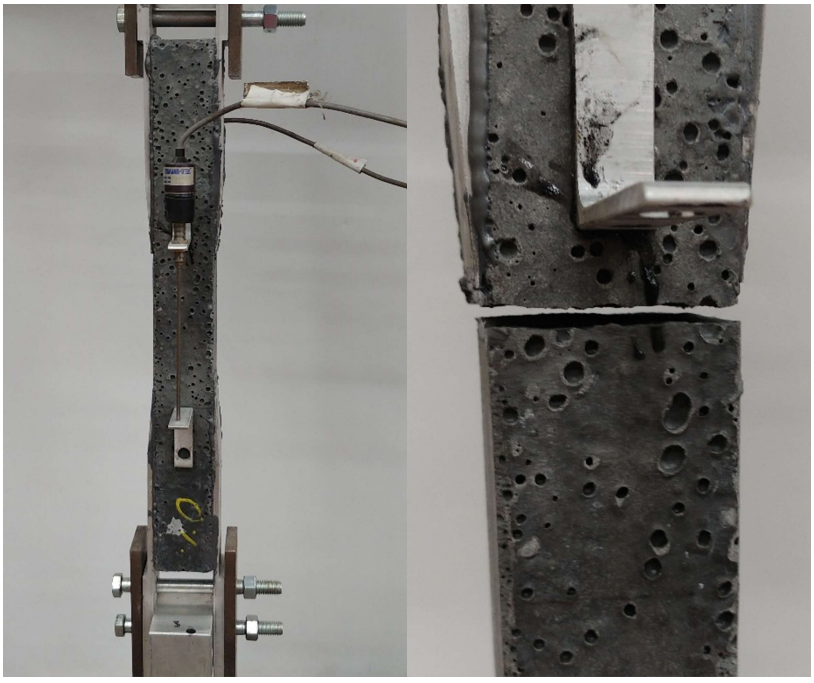

Figure 4.2.2. 3 Crack pattern 0% steel fiber content Specimen 3

Figures 4.2.2.4, 4.2.2.5, and 4.2.2.6 show the cracking pattern that developed throughout the direct tensile test for the 1% steel fiber specimens. All of the specimens cracked within the LVDT instrumented gauge length which allowed for the direct tensile stress-average strain curve to be fully captured. In each case, the crack developed nonuniformly throughout the specimen. After the first crack developed, the fibers bridged the crack resulting in a nonuniform crack pattern. In Figure 4.2.2.6 it is observed that after the specimen had been completely pulled apart, the exposed steel fibers measured to half the initial fiber length. From Figure 4.2.2.4 it is shown that the crack formed near the aluminum plates for specimen 1. Figures 4.2.2.5 and 4.2.2.6 shows that the crack formed near the middle for specimens 1 and 2.

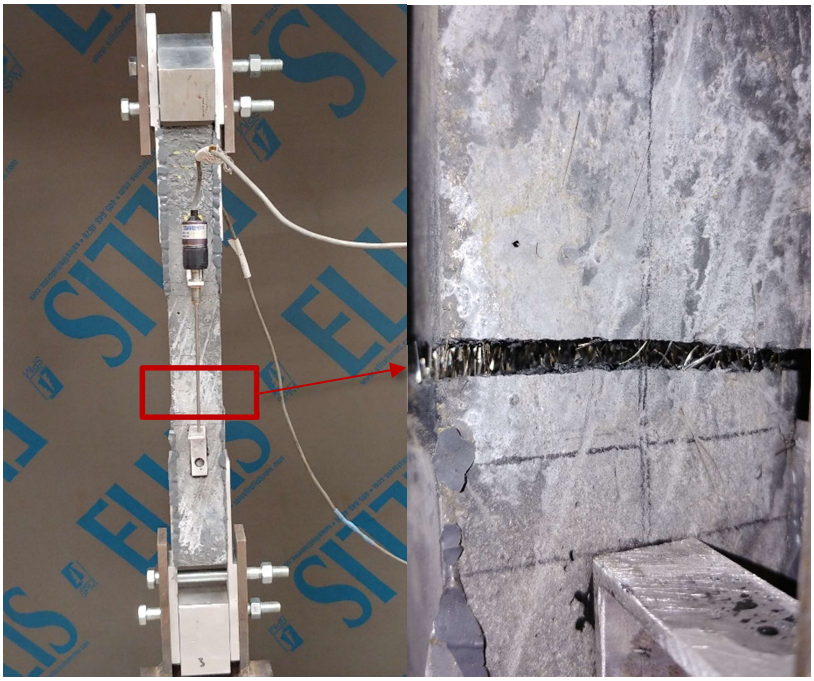

Figure 4.2.2. 4 Crack pattern 1% steel fiber content Specimen 1

Figure 4.2.2. 5 Crack pattern 1% steel fiber content Specimen 2

Figure 4.2.2. 6 Crack pattern 1% steel fiber content Specimen 3

Figures 4.2.2.7, 4.2.2.8, and 4.2.2.9 show the cracking pattern that developed throughout the direct tensile test for the 2% steel fiber specimens. All of the specimens cracked within the LVDT instrumented gauge length which allowed for the direct tensile stress-average strain curve to be fully captured. In general, multiple cracks developed near the first crack until one of the cracks began to widen (crack localization). After the post-cracking strength was attained, the bridging of the steel fibers would hold the specimen together until the specimen was completely pulled apart. All of the specimens failed near the aluminum plates. From Figure 4.2.2.7 it is shown that for specimen 1, one crack formed near the aluminum plates and then a second crack formed near the middle of the specimen. Because the initial crack that formed near one of the aluminum plates ended in the gripping zone, the epoxied aluminum plate and UHPC that did not have cracks was able to impose a stress concentration which allowed a second micro crack to widen near the middle of the specimen. Consequently, specimen 1 misaligned with the universal testing machine which rotated the specimen. Specimens 2 and 3 had similar cracking patterns to the 1% steel fiber specimens.

Figure 4.2.2. 7 Crack pattern 2% steel fiber content Specimen 1

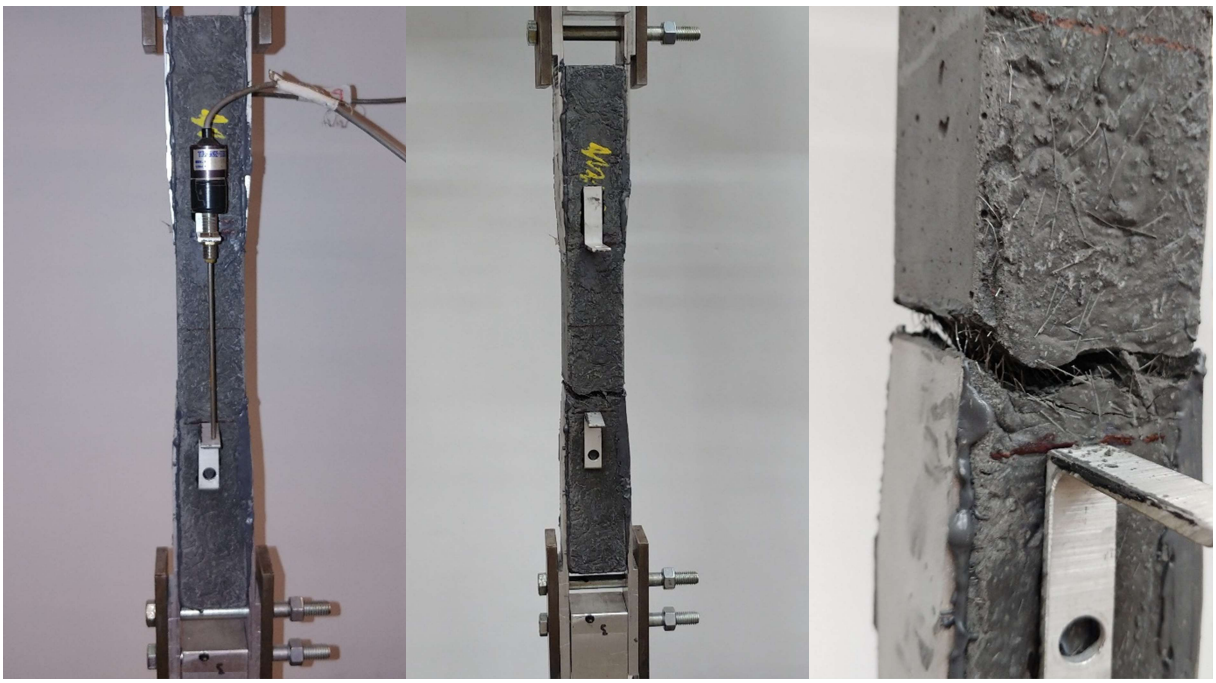

Figure 4.2.2. 8 Crack pattern 2% steel fiber content Specimen 2

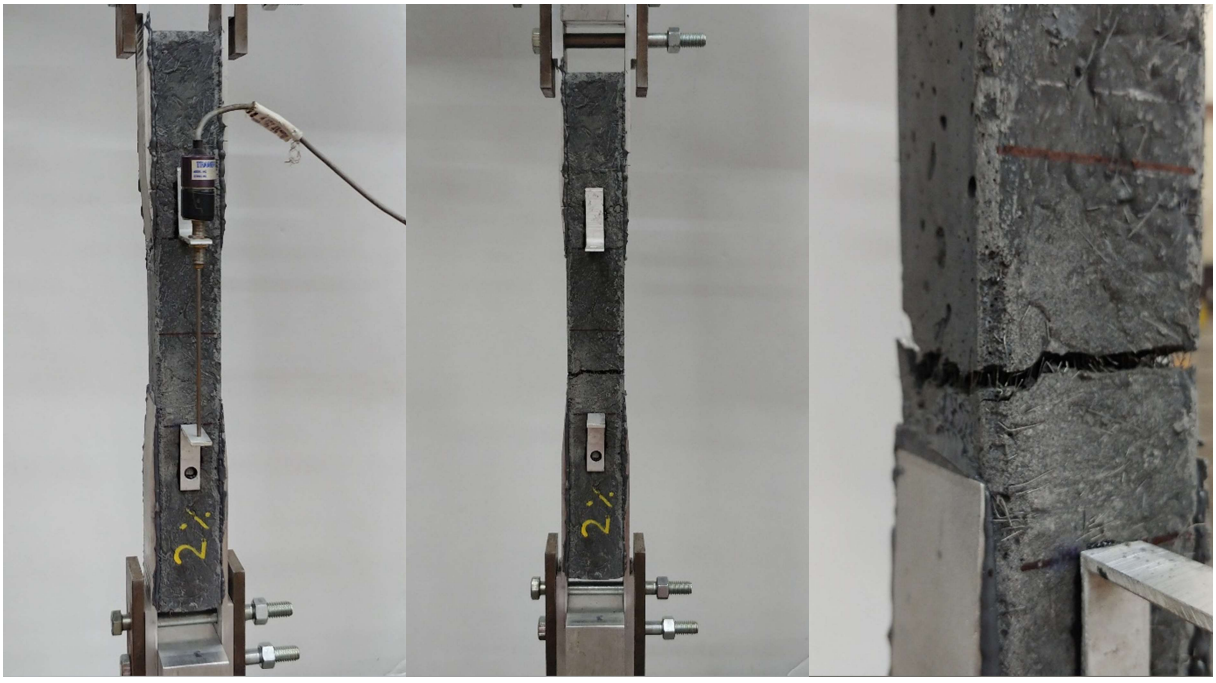

Figure 4.2.2. 9 Crack pattern 2% steel fiber content Specimen 3

Figures 4.2.2.10, 4.2.2.11, and 4.2.2.12 show the cracking pattern that developed throughout the direct tensile test for the 4% steel fiber specimens. All of the specimens cracked within the LVDT instrumented gauge length which allowed for the direct tensile stress-average strain curve to be fully captured. In general, multiple cracks developed near the first crack until one of the cracks began to widen. After the post-cracking strength was attained, the bridging of the steel fibers would hold the specimen together until the specimen was completely pulled apart. All of the 4% specimens failed near the aluminum plates. The crack patterns in specimens 1, 2, and 3 are all similar. In each case the localized crack developed by connecting multiple surrounding cracks. Although uniform cracks did form around the localized crack, the localized crack did not form uniformly throughout the specimen. The nonuniform localized cracks observed in the 4% steel fiber specimens is potentially due fiber distribution.

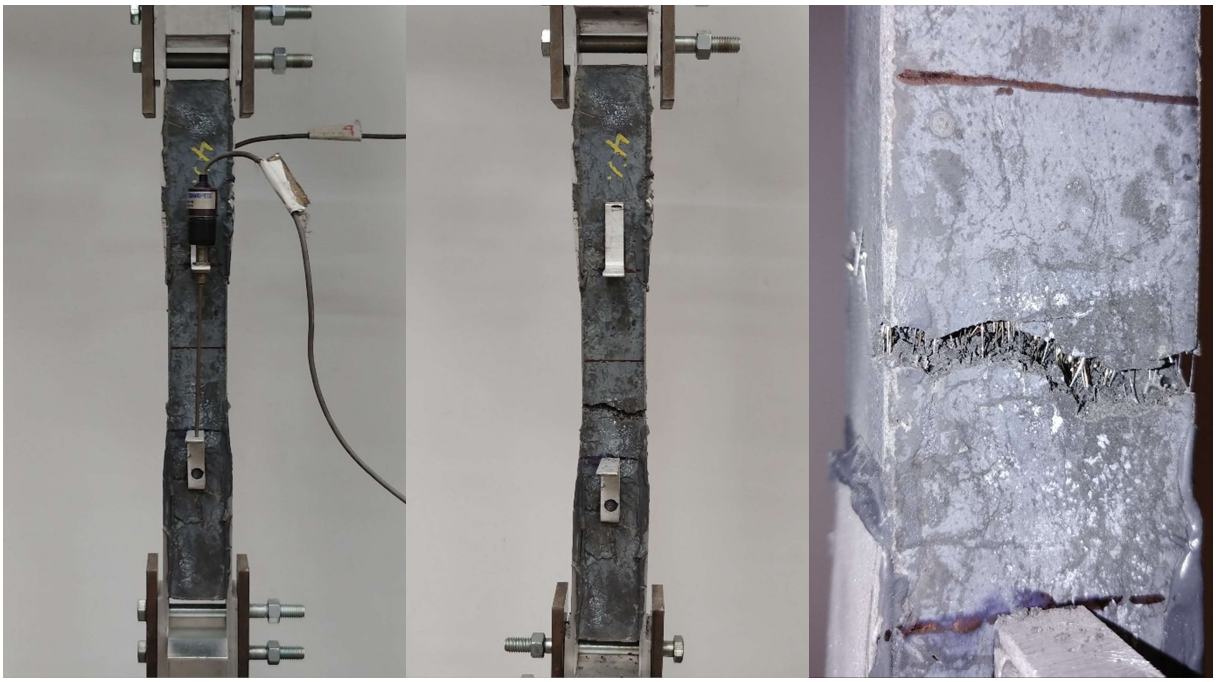

Figure 4.2.2. 10 Crack pattern 4% steel fiber content Specimen 1

Figure 4.2.2. 11 Crack pattern 4% steel fiber content Specimen 2

Figure 4.2.2. 12 Crack pattern 4% steel fiber content Specimen 3

Figures 4.2.2.13, 4.2.2.14, and 4.2.2.15 show the cracking pattern that developed throughout the direct tensile test for the 6% steel fiber specimens. All of the specimens cracked within the LVDT instrumental gauge length which allowed for the direct tensile stress-average strain curve to be fully captured. In general, multiple cracks, observed from the stress-strain curve, developed near the first crack until one of the cracks began to widen. After the post-cracking strength was attained, the bridging of the steel fibers would hold the specimen together until the specimen was completely pulled apart. Only one specimen failed near the aluminum plates and the other two failed near the center. The crack pattens in specimens 1, 2, and 3 are all similar to the 4% steel fiber specimens.

Figure 4.2.2. 13 Crack pattern 6% steel fiber content Specimen 1

Figure 4.2.2. 14 Crack pattern 6% steel fiber content Specimen 2

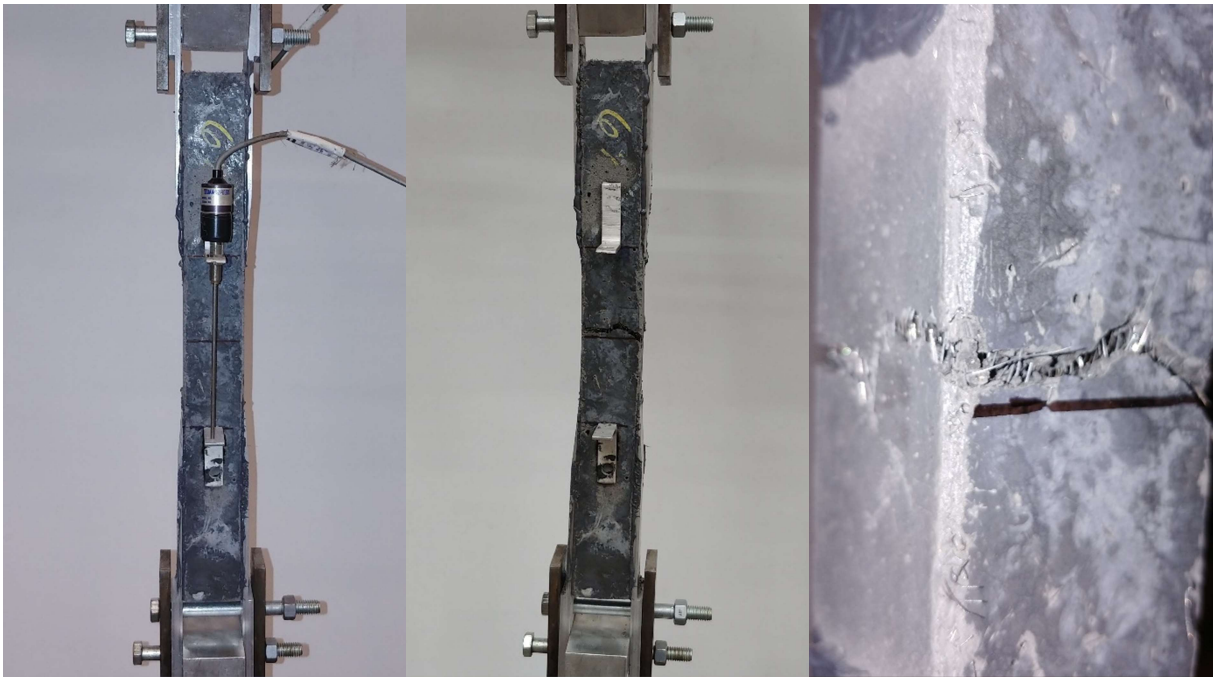

Figure 4.2.2. 15 Crack pattern 6% steel fiber content Specimen 3

4.2.3 0% Steel Fibers

The stress-average strain curves of the 0% steel fiber content direct tensile specimen tests are shown in Figure 4.2.3.1. At a steel fiber content of 0%, the first crack stress was observed to be the maximum tensile stress. From Figure 4.2.3.1 it is observed that the direct tensile first crack stress occurs before a strain of 0.0003 is achieved and after the elastic region. An average stress-strain curve for 0% steel fiber content is shown in Figure 4.2.3.2.

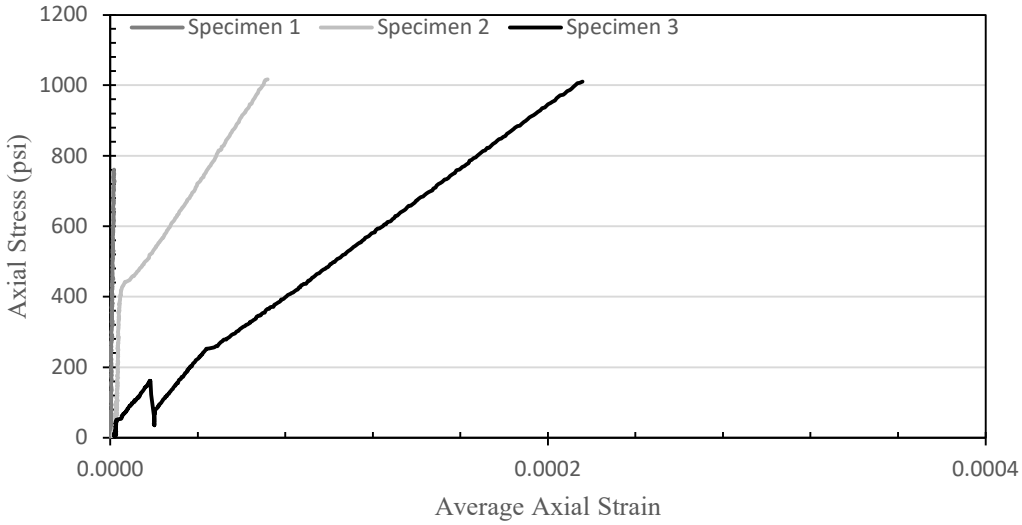

Figure 4.2.3. 1 Stress-strain response for 0% steel fiber content direct tensile specimens: elastic and first crack region

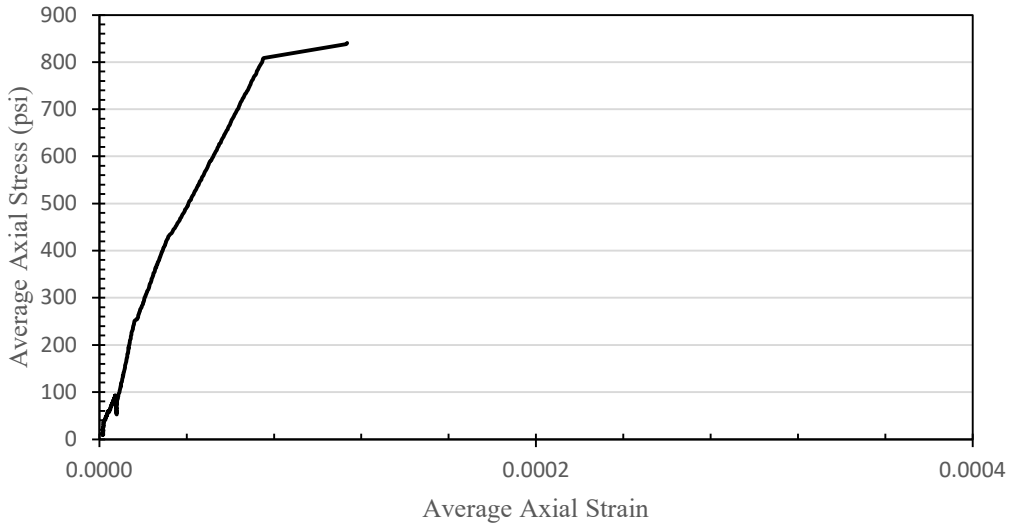

Figure 4.2.3. 2 Average stress-strain response for 0% steel fiber content direct tensile specimens: elastic and first crack region

4.2.4 1% Steel Fibers

The stress-average strain curves of the 1% steel fiber content direct tensile specimen tests are shown in Figures 4.2.4.1 and 4.2.4.2. The first crack stress for 1% steel fiber content was observed to be equivalent to the post-cracking stress. From Figure 4.2.4.1 it is observed that the direct tensile first crack stress occurs before a strain of 0.0003 is achieved and after the elastic region. After the first crack, strain softening occurs until the steel fibers pullout and the specimen fails in direct tension. Figure 4.2.4.2 shows that after the first crack occurs, the tensile strength of the specimens generally decreases linearly as the first crack widens and the steel fibers bridge the gap. An average stress-strain curve for 1% steel fiber content is shown in Figures 4.2.4.3 and 4.2.4.4.

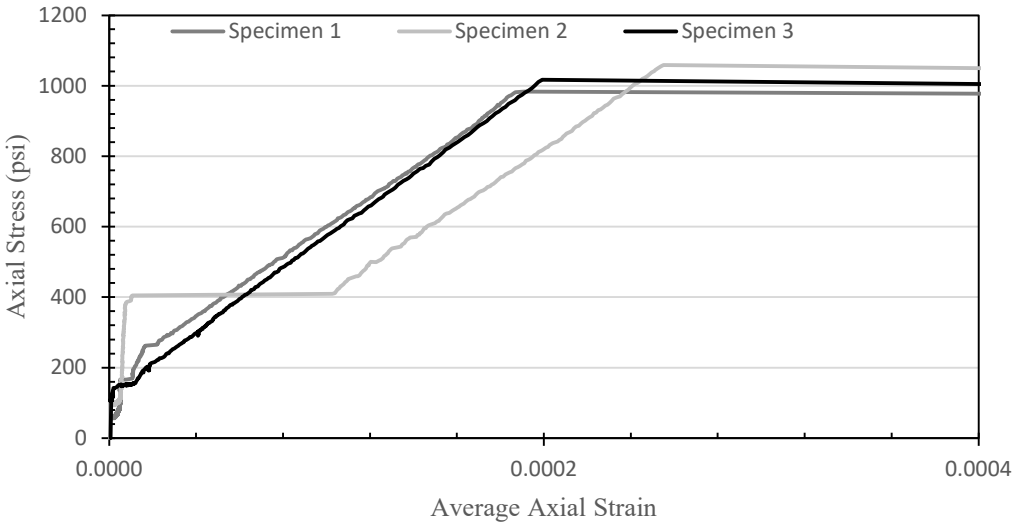

Figure 4.2.4. 1 Stress-strain response for 1% steel fiber content direct tensile specimens: elastic and first crack region

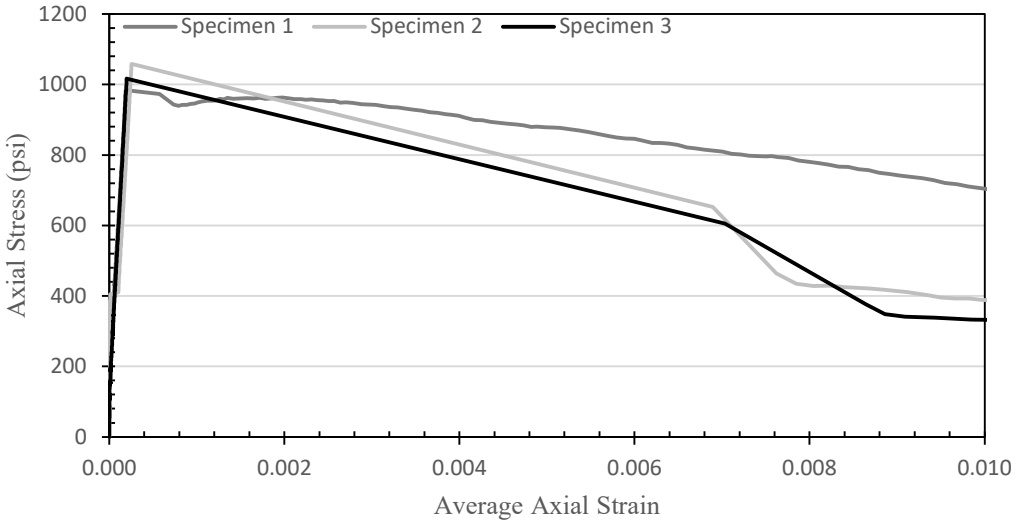

Figure 4.2.4. 2 Stress-strain response for 1% steel fiber content direct tensile specimens: full direct tensile behavior region

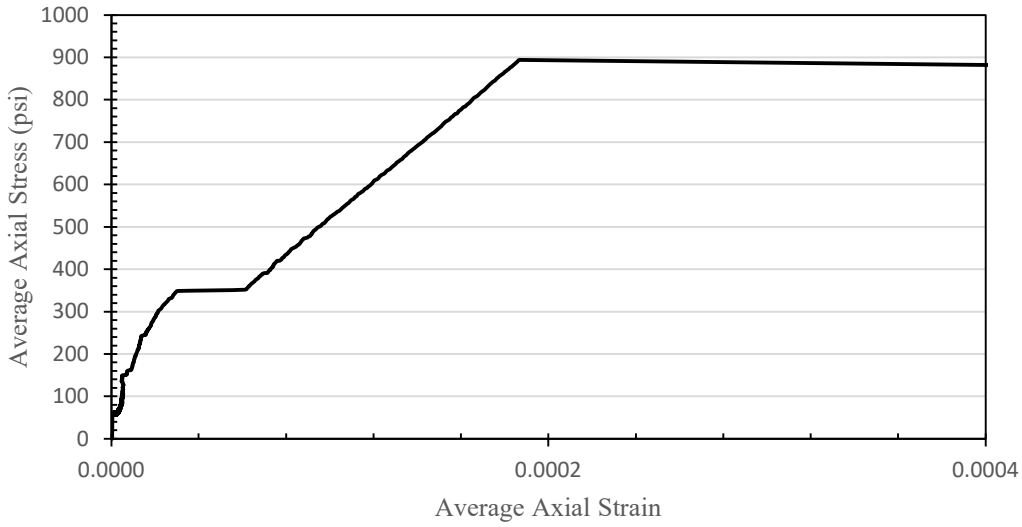

Figure 4.2.4. 3 Average stress-strain response for 1% steel fiber content direct tensile specimens: elastic and first crack region

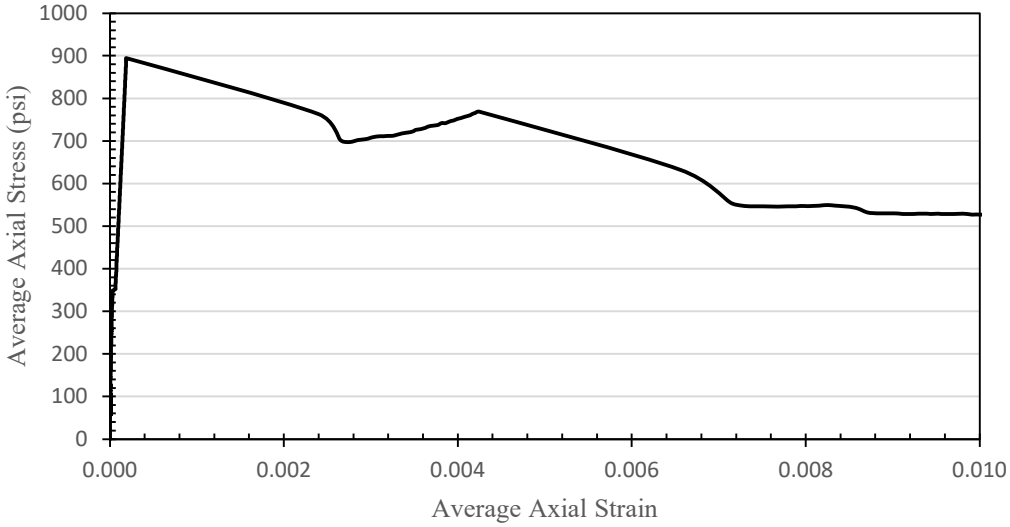

Figure 4.2.4. 4 Average stress-strain response for 1% steel fiber content direct tensile specimens: full direct tensile behavior region

4.2.5 2% Steel Fibers

The stress-average strain curves of the 2% steel fiber content direct tensile specimen tests are shown in Figures 4.2.5.1 and 4.2.5.2. Unlike the 1% steel fiber specimens, the post-cracking stress for the 2% steel fiber specimens exceeded the first crack stress. From Figure 4.2.5.1 it is observed that the direct tensile first crack stress occurs before a strain of 0.0003 is achieved and after the elastic region. After the first crack, strain hardening, multi-cracking, and steel fiber bridging occurs until the post-cracking strength (steel fiber bridging strength) is attained. Figure 4.2.5.1 shows that during strain hardening, the tensile stress-strain curve generally increases as the steel fibers bridge the cracks until the post-cracking stress is reached. After the post-cracking stress is attained, strain softening and steel fiber pullout occurs until the steel fibers completely pullout. An average stress-strain curve for 2% steel fiber content is shown in Figures 4.2.5.3 and 4.2.5.4.

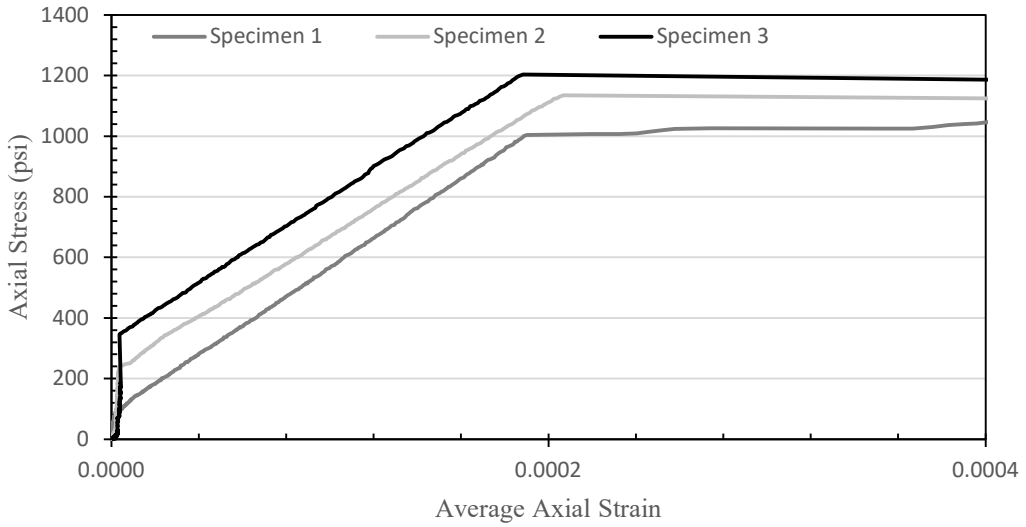

Figure 4.2.5. 1 Stress-strain response for 2% steel fiber content direct tensile specimens: elastic and first crack region

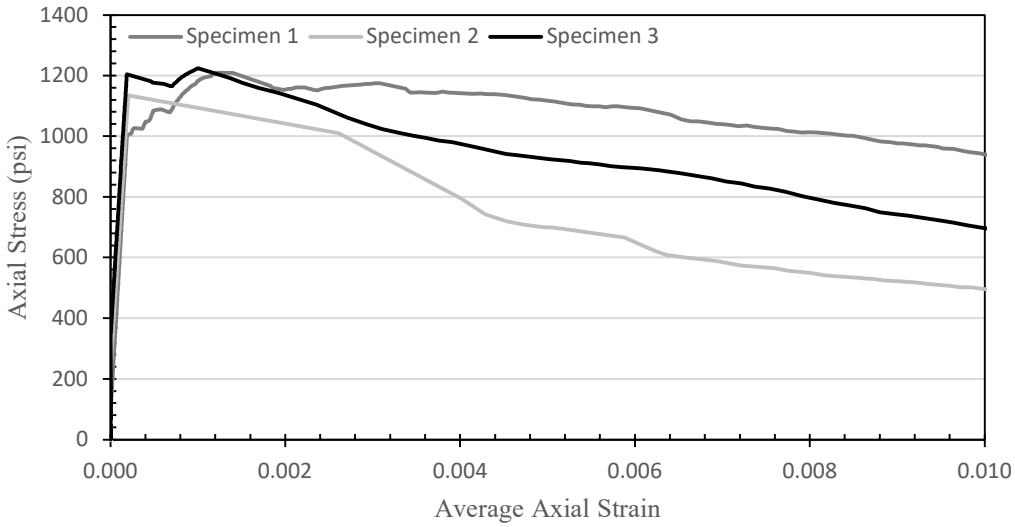

Figure 4.2.5. 2 Stress-strain response for 2% steel fiber content direct tensile specimens: full direct tensile behavior region

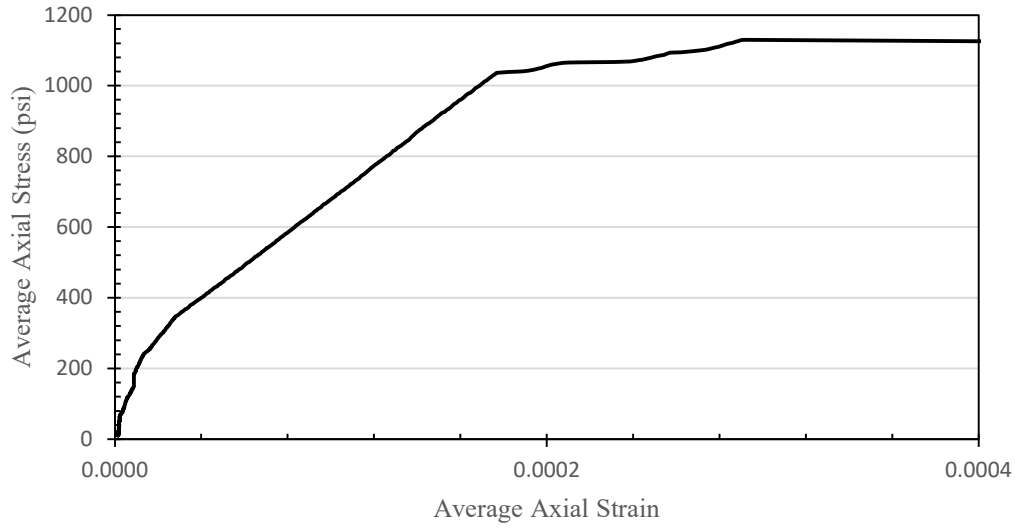

Figure 4.2.5. 3 Average stress-strain response for 2% steel fiber content direct tensile specimens: elastic and first crack region

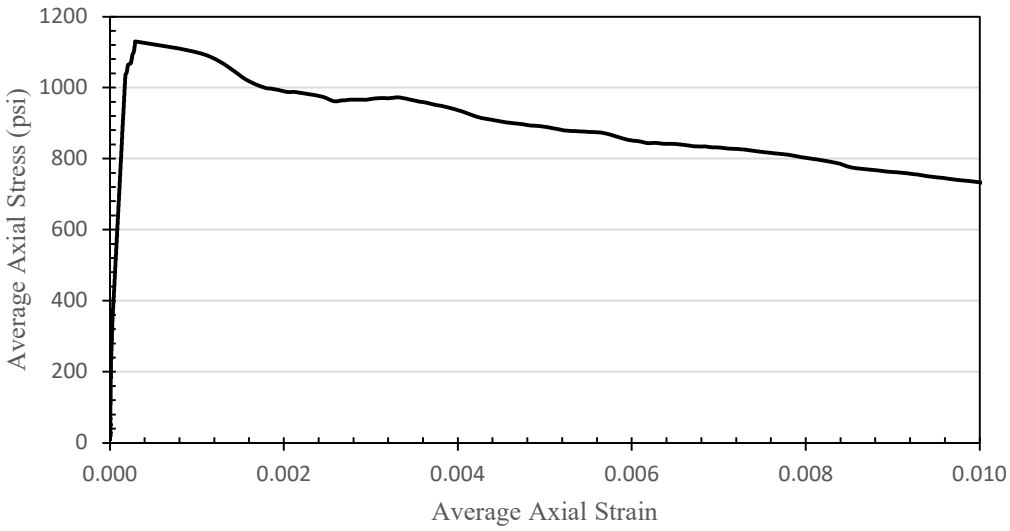

Figure 4.2.5. 4 Average stress-strain response for 2% steel fiber content direct tensile specimens: full direct tensile behavior region

4.2.6 4% Steel Fibers

The stress-average strain curves of the 4% steel fiber content direct tensile specimen tests are shown in Figures 4.2.6.1 and 4.2.6.2. The post-cracking stress for the 4% steel fiber specimens exceeded the first crack stress. From Figure 4.2.6.1 it is observed that the direct tensile first crack stress occurs before a strain of 0.0003 is achieved and after the elastic region. After the first crack, strain hardening, multi-cracking, and steel fiber bridging occurs until the post-cracking strength (steel fiber bridging strength) is attained. Figure 4.2.6.1 shows that during strain hardening, the tensile stress-strain curve generally increases as the steel fibers bridge the cracks until the post-cracking stress is reached. Comparatively, the strain hardening region at 4% steel fiber content is more evident than at 2% steel fiber content. After the maximum post-cracking stress is attained, strain softening and steel fiber pullout occurs until the steel fibers completely pullout. An average stress-strain curve for the 4% steel fiber content is shown in Figures 4.2.6.3 and 4.2.6.4.

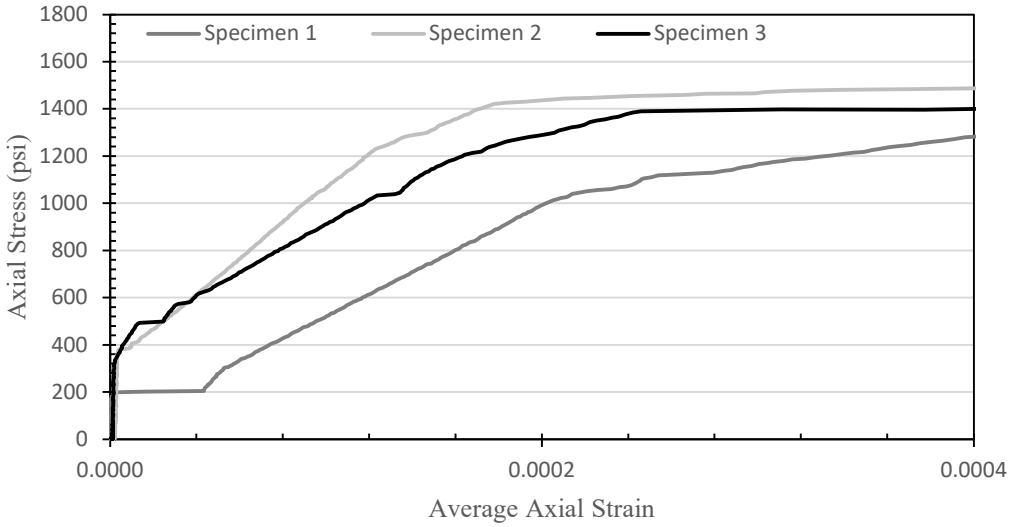

Figure 4.2.6. 1 Stress-strain response for 4% steel fiber content direct tensile specimens: elastic and first crack region

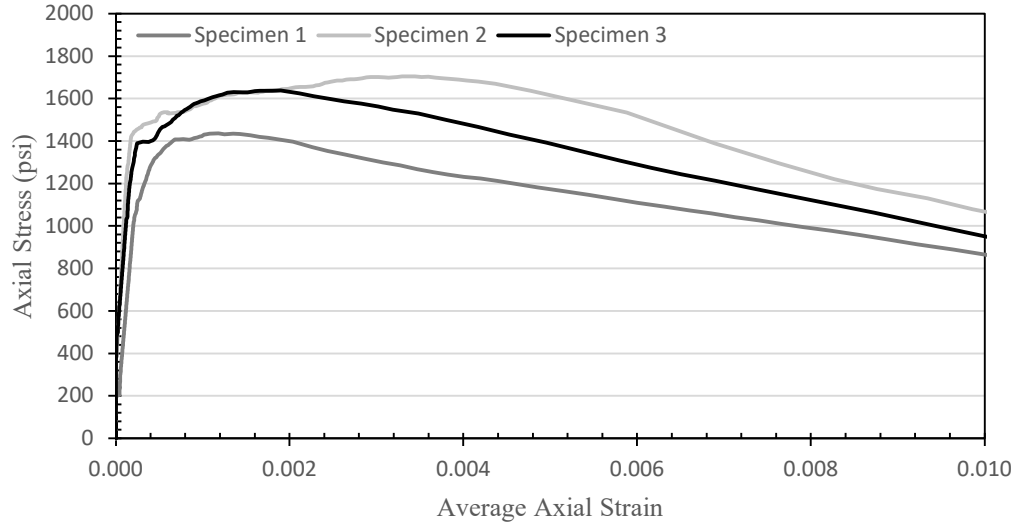

Figure 4.2.6. 2 Stress-strain response for 4% steel fiber content direct tensile specimens: full direct tensile behavior region

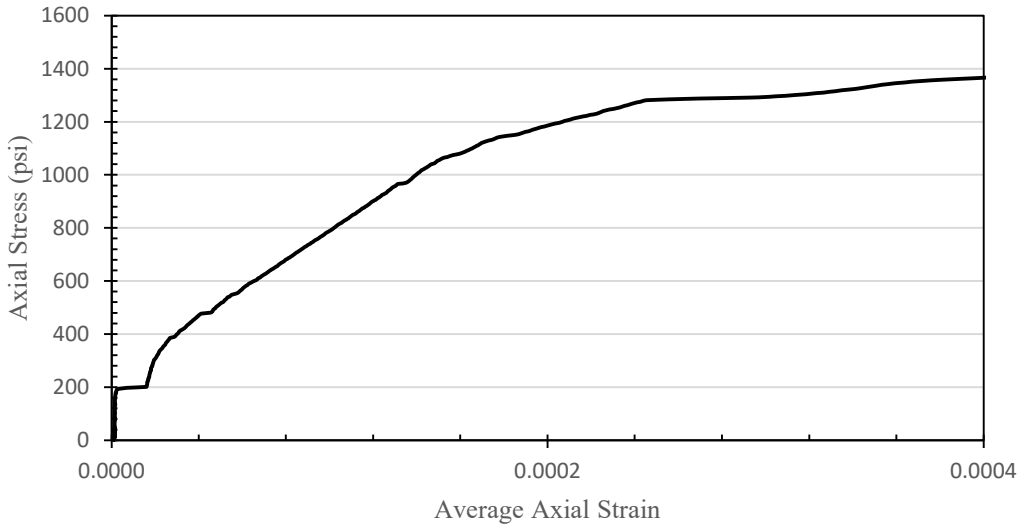

Figure 4.2.6. 3 Average stress-strain response for 4% steel fiber content direct tensile specimens: elastic and first crack region

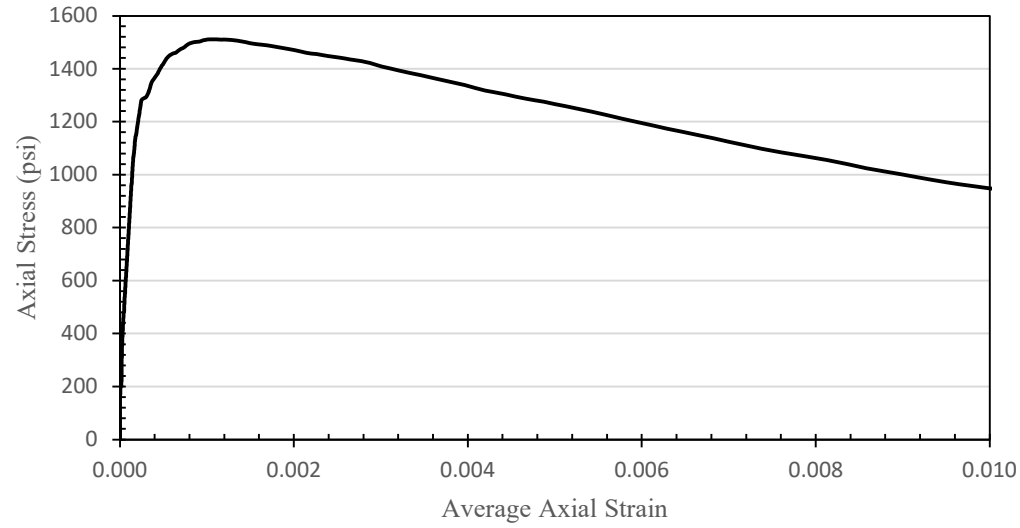

Figure 4.2.6. 4 Average stress-strain response for 4% steel fiber content direct tensile specimens: full direct tensile behavior region

4.2.7 6% Steel Fibers

The stress-average strain curves of the 6% steel fiber content direct tensile specimen tests are shown in Figures 4.2.7.1 and 4.2.7.2. The post-cracking stress for the 6% steel fiber specimens exceeded the first crack stress. From Figure 4.2.7.1 it is observed that the direct tensile first crack stress occurs before a strain of 0.0002 is achieved and after the elastic region. The lower first crack strain can be attributed to the higher tensile modulus of elasticity due to an increased steel fiber content. After the first crack, strain hardening, multi-cracking, and steel fiber bridging occurs until the post-cracking strength (steel fiber bridging strength) is attained. Figure 4.2.7.1 shows that during strain hardening, the tensile stress-strain curve generally increases as the steel fibers bridge the cracks until the post-cracking stress is reached. After the post-cracking stress is attained, strain softening and steel fiber pullout occurs until the steel fibers completely pullout. Due to uneven fiber distribution and poor consolidation, a complex stress distribution develops between the UHPC and the steel fibers resulting in the development of stress concentrations and uneven steel fiber pullout during the strain hardening region. The fiber pullout continues throughout the strain hardening region until the uneven fiber distribution returns to equilibrium. The loss of steel fibers during the hardening region results in a post-cracking strength that is lower than expected. This phenomena does not affect the first crack strength as this happens after the elastic region. An average stress-strain curve for the 6% steel fiber content is shown in Figures 4.2.7.3 and 4.2.7.4.

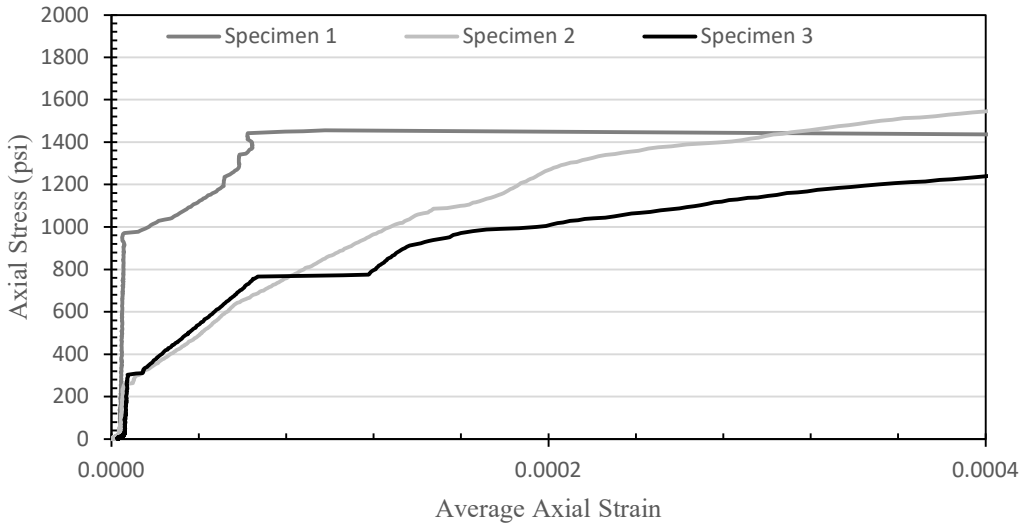

Figure 4.2.7. 1 Stress-strain response for 6% steel fiber content direct tensile specimens: elastic and first crack region

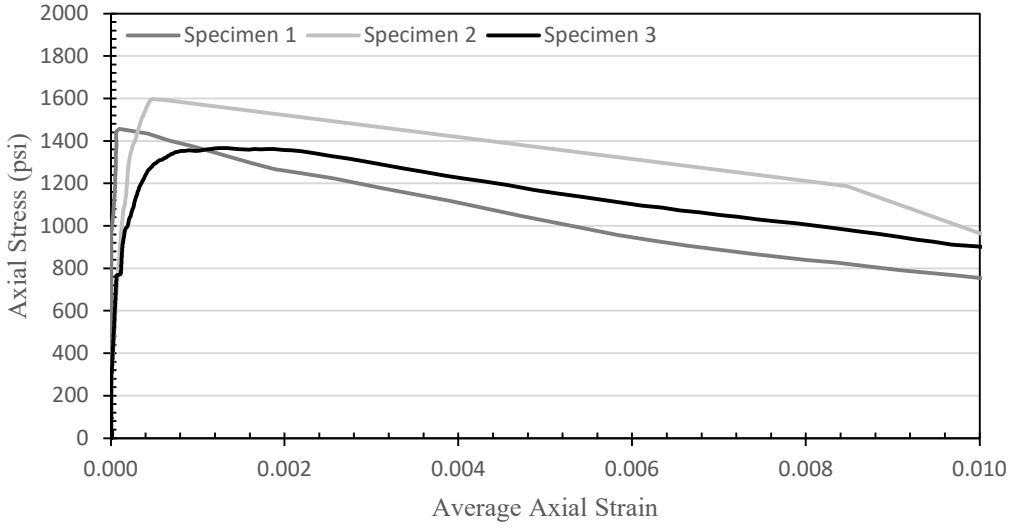

Figure 4.2.7. 2 Stress-strain response for 6% steel fiber content direct tensile specimens: full direct tensile behavior region

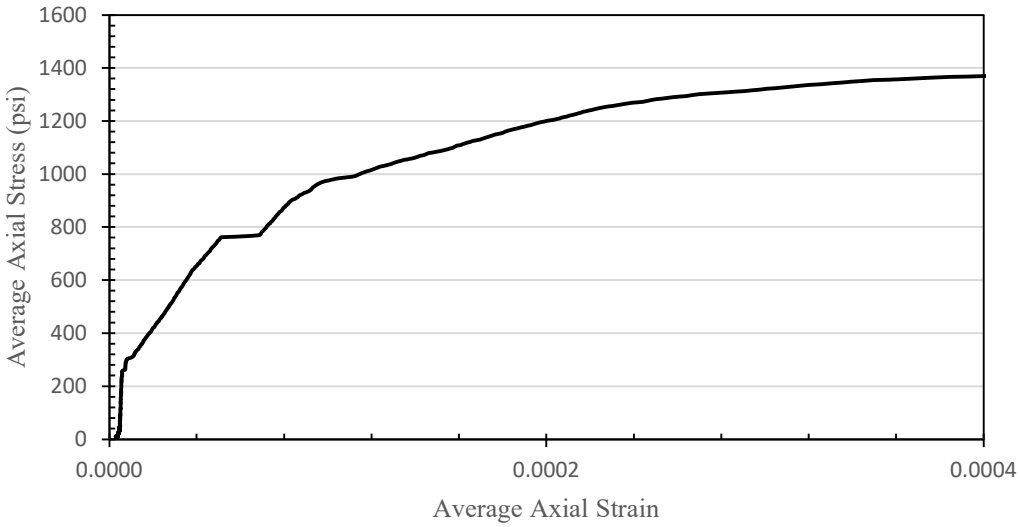

Figure 4.2.7. 3 Average stress-strain response for 6% steel fiber content direct tensile specimens: elastic and first crack region

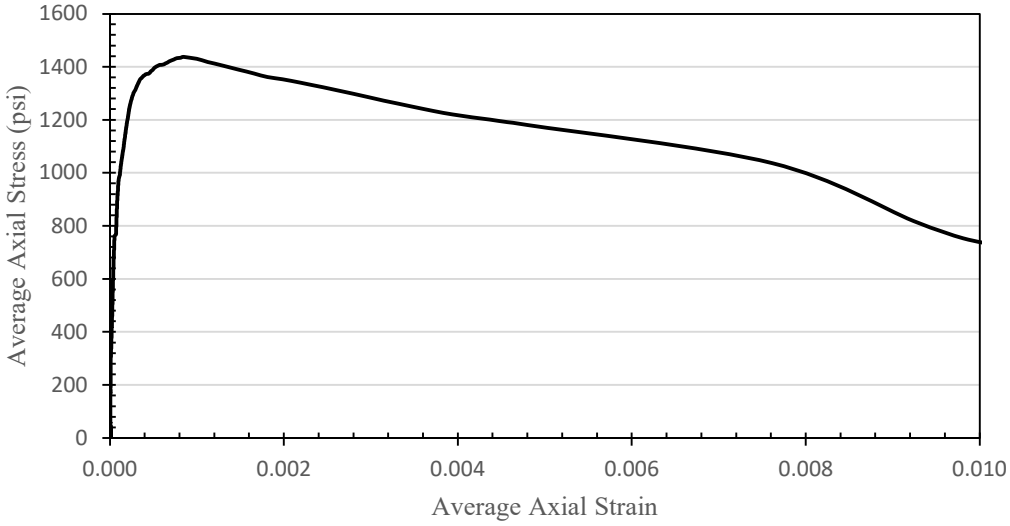

Figure 4.2.7. 4 Average stress-strain response for 6% steel fiber content direct tensile specimens: full direct tensile behavior region

4.2.8 Average Stress-Strain Curve for J3-UHPC

The average stress-strain curves of 0%, 1%, 2%, 4%, and 6% steel fiber content direct tensile tests are shown in Figures 4.2.8.1 and 4.2.8.2. From Figure 4.2.8.1 it is observed that the fiber distribution phenomena for 6% steel fiber content begins at the first crack strength and continues until the remaining fibers are distributed evenly. The 6% stress-strain curve is shown to momentarily exhibit 4% steel fiber content characteristics after a strain of 0.00016 during the strain hardening region. Figure 4.2.8.2 also shows that the decreasing tensile strength in the strain softening region stabilizes with increasing steel fiber content, due to steel fiber bridging. The 0% steel fiber content stress-strain curve is seen to end before the 1%, 2%, 4%, and 6% fiber contents which shows that including steel fibers allows the J3-UHPC to attain a post-cracking stress. Furthermore, increasing the steel fiber content from 2% to 4% is seen to also increase the post-cracking stress.

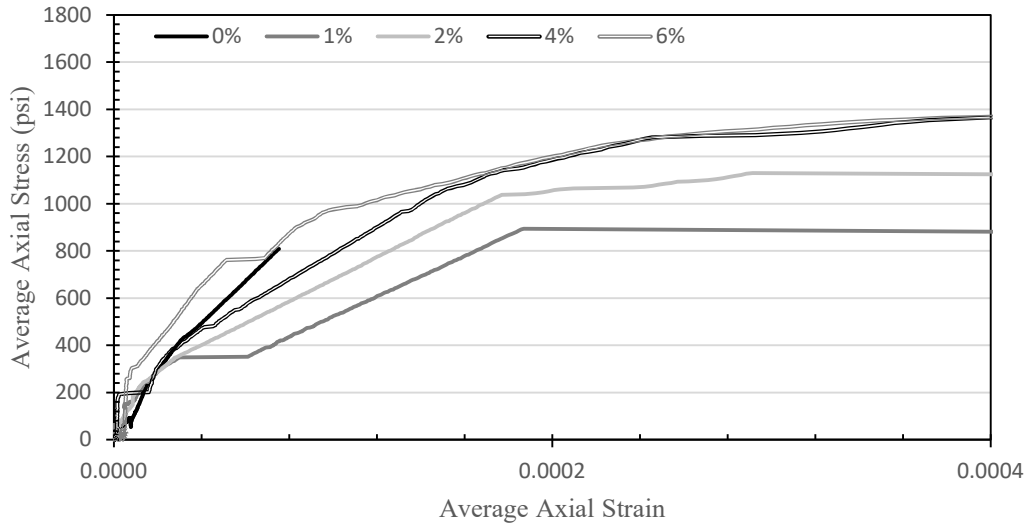

Figure 4.2.8. 1 Average stress-strain response for 0%, 1%, 2%, 4%, and 6% steel fiber contents: elastic and first crack region

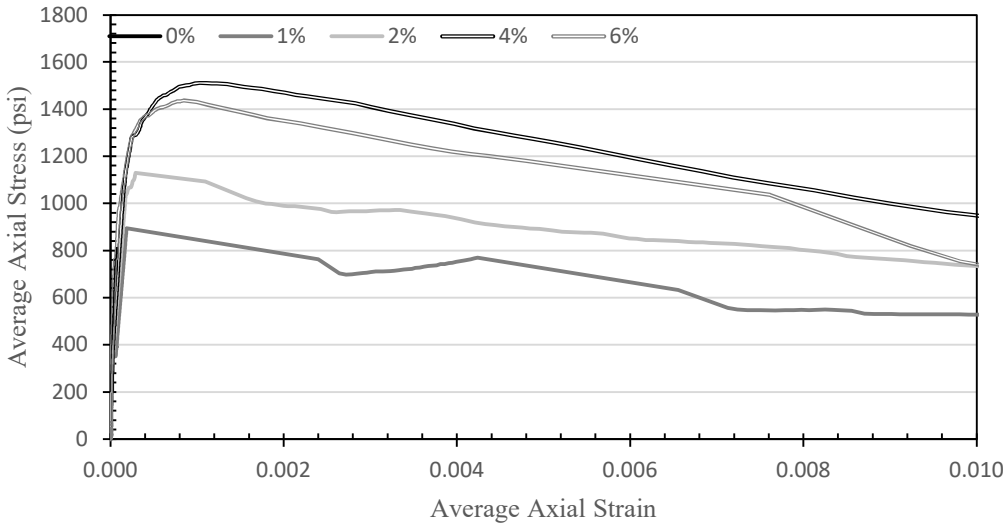

Figure 4.2.8. 2 Average stress-strain response for 0%, 1%, 2%, 4%, and 6% steel fiber contents: full direct tensile behavior region

From the average 0% and 1% stress-strain curves, an idealized average stress-strain curve that illustrates the observed mechanical characteristics of J3-UHPC was developed and is shown in Figure 4.2.8.3. It is important to note that the 0% steel fiber specimens do not experience strain softening and the strain softening region only applies to 1% steel fiber specimens. From the average 2%, 4% and 6% stress-strain curves, an idealized average stress-strain curve that illustrates the observed mechanical characteristics of J3-UHPC was developed and is shown in Figure 4.2.8.4. In Figure 4.2.8.3 the first crack stress (σ_{fc}) is defined as the stress at which the first crack is observed. The first crack occurs generally at the end of the elastic region. The first crack strain (ε_{fc}) is defined as the strain that corresponds to the first crack stress. In Figure 4.2.8.4 the post-cracking stress (σ_{pc}) is defined as the maximum tensile stress after the multi-cracking region. The post-cracking strain (ε_{pc}) is defined as the strain that corresponds to the post-cracking stress. It is important to note that the strain hardening and strain softening regions are nonlinear by definition, however, they are illustrated as linear in Figures 4.2.8.3 and 4.2.8.4 for simplicity.

Furthermore, the tensile assembly may need to be modified to capture the true strain hardening and strain softening of J3-UHPC. Figure 4.2.8.2 shows that the strain softening may not be fully captured potentially due to the hinges in the testing assembly.

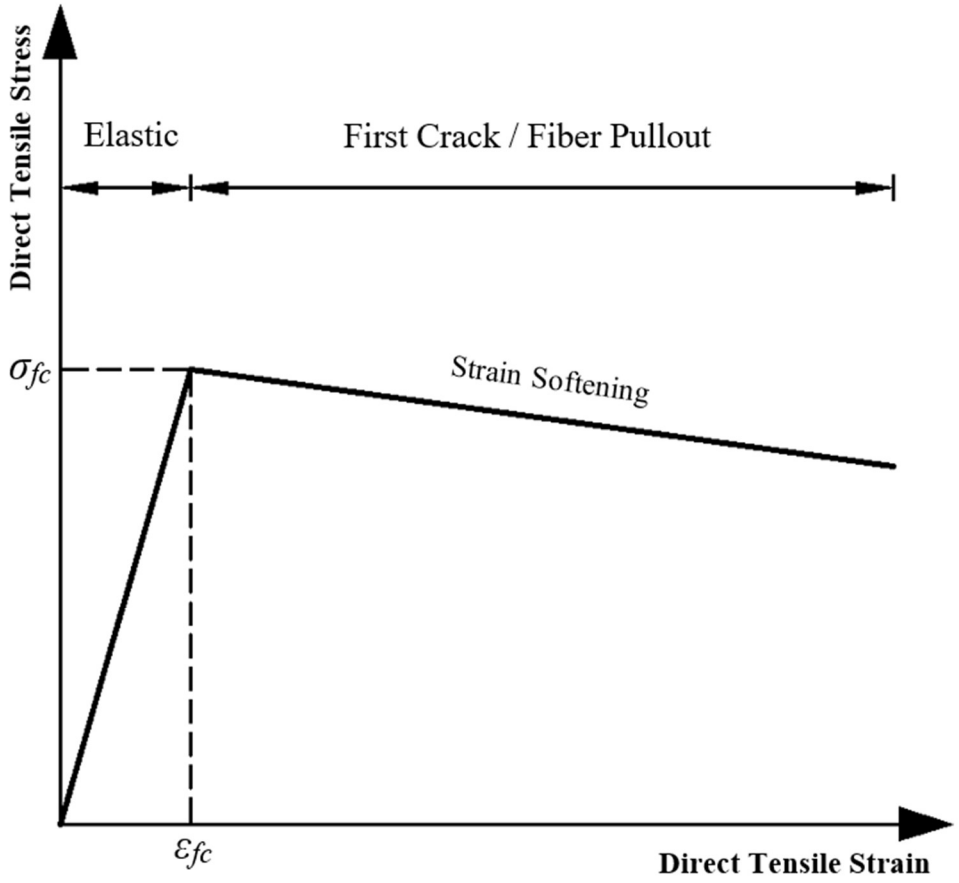

Figure 4.2.8. 3 Idealized UHPC direct tensile stress-strain response for 0% and 1% steel fiber contents

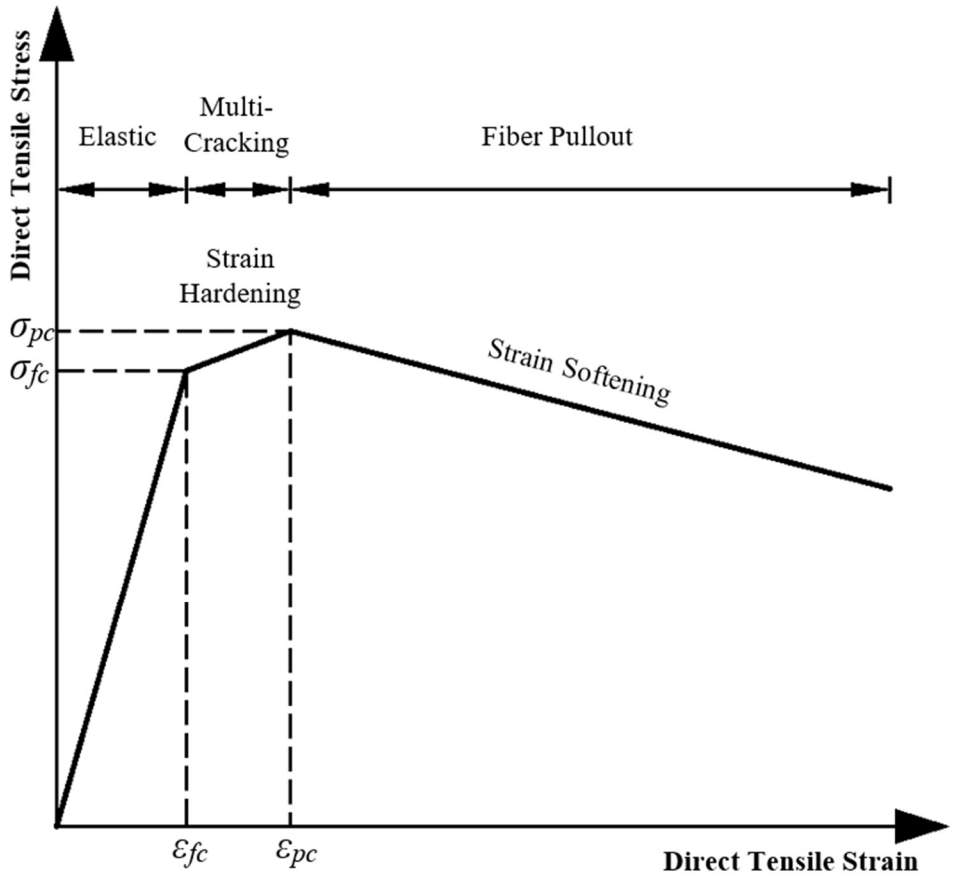

Figure 4.2.8. 4 Idealized UHPC direct tensile stress-strain response for 2%, 4%, and 6% steel fiber contents

4.3 Regression Models

4.3.1 Splitting Tensile Strength Correlations

The multivariable nonlinear regression model, based on the power model, that correlates the compressive strength and steel fiber content with the splitting tensile strength is

$$f_{st} = 1.69\text{x}10^{9}(f_c)^{-3.673}(1 + 2.07\text{x}10^{9}(V_f)) + 1{,}239 \qquad \text{(Eq. 4.3.1.1)}$$

where,

$f_{st} = splitting$ tensile $strength$ (psi)

$f_c = compressive\ strength$ (psi) and

$V_f = volumetric\ steel\ fiber\ content$ (%)

The constants that are incorporated into Eq. 4.3.1.1 were derived from regression analysis. Figure 4.3.1.1 shows that there is a strong correlation between the splitting tensile strength, compressive strength, and steel fiber content. The predicted splitting tensile values produced by Eq. 4.3.1.1 trend accurately with the measured splitting tensile strengths resulting in a model that predicts realistic strengths. The RMSE is 183.7 psi and the coefficient of determination is 0.93 for Eq. 4.3.1.1.

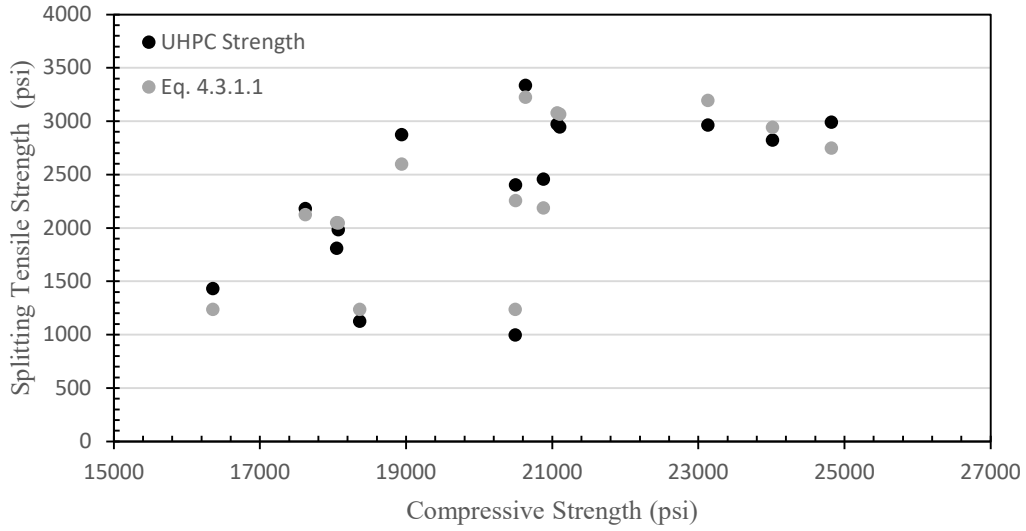

Figure 4.3.1. 1 Splitting tensile strength vs. compressive strength: comparison of measured strengths and predicted strengths

The multivariable nonlinear regression model, based on the power model, that correlates the flexural strength and the steel fiber content with the splitting tensile strength is

$$f_{st} = 54{,}392(f_r)^{0.017}\left(1 + 0.001\left(V_f\right)\right) - 59{,}764 \qquad \text{(Eq. 4.3.1.2)}$$

where,

$f_{st} = splitting$ tensile $strength$ (psi)

$f_r = flexural\ strength$ (psi) and

$V_f = volumetric\ steel\ fiber\ content$ (%)

The constants that are incorporated into Eq. 4.3.1.2 were derived from regression analysis. Figure 4.3.1.2 shows that there is a correlation between the splitting tensile strength, flexural strength, and steel fiber content. The predicted splitting tensile values produced by Eq. 4.3.1.2 trend with the measured splitting tensile strengths resulting in a model that predicts realistic strengths. The RMSE is 343.0 psi and the coefficient of determination is 0.81 for Eq. 4.3.1.2. The root mean square error and R^2 (coefficient of determination) analysis is shown in Table 4.3.1.1.

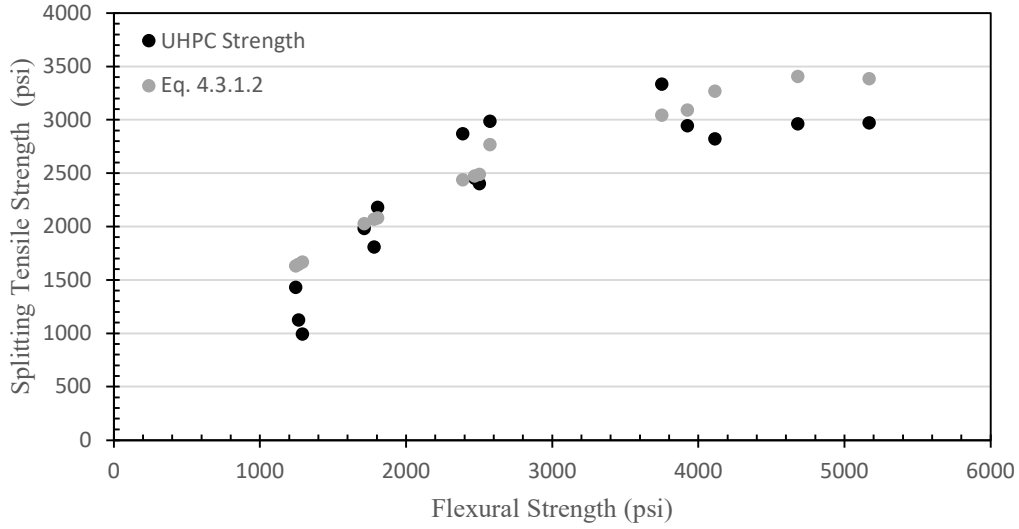

Figure 4.3.1. 2 Splitting tensile strength vs. flexural strength: comparison of measured strengths and predicted strengths

Table 4.3.1. 1 Splitting tensile strength root mean square error analysis

Equation	RMSE	R^2
Eq. 4.3.1.1	183.7	0.93
Eq. 4.3.1.2	343.0	0.81

Note: RMSE = root mean square error (psi), R^2 = coefficient of determination

4.3.2 Flexural Strength Correlations

The multivariable nonlinear regression model, based on the power model, that correlates the compressive strength and steel fiber content with the flexural strength is

$$f_r = 2.61\text{x}10^7(f_c)^{-2.8}(1 + 3.5(V_f)) + 973 \qquad \text{(Eq. 4.3.2.1)}$$

where,

$f_r = flexural\ strength$ (psi)

$f_c = compressive\ strength$ (psi) and

$V_f = volumetric\ steel\ fiber\ content$ (%)

The constants that are incorporated into Eq. 4.3.2.1 were derived from regression analysis. Figure 4.3.2.1 shows that there is a correlation between the flexural strength, compressive strength, and steel fiber content. The predicted flexural values produced by Eq. 4.3.2.1 trend accurately with the measured flexural strengths resulting in a model that predicts realistic strengths. The RMSE is 525.2 psi and the coefficient of determination is 0.82 for Eq. 4.3.2.1.

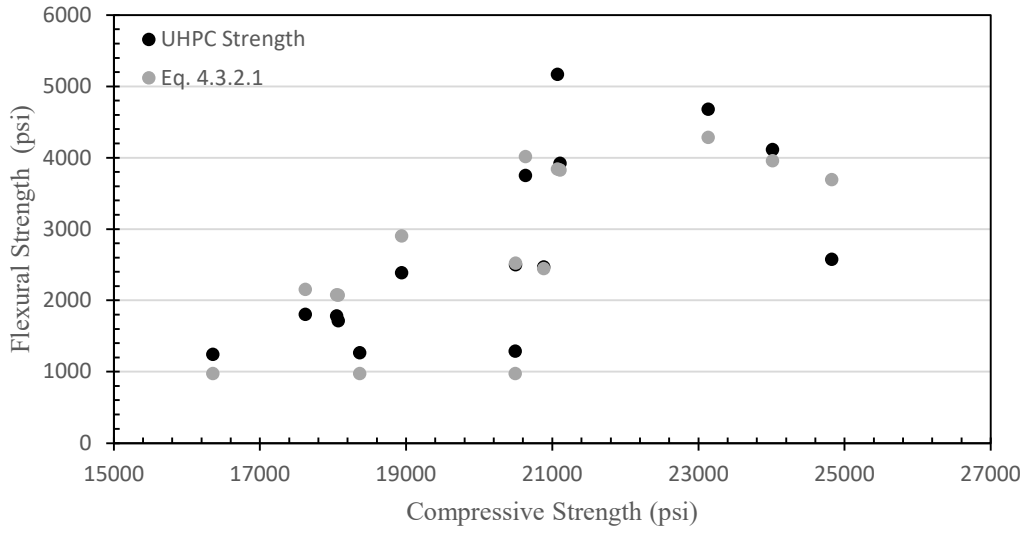

Figure 4.3.2. 1 Flexural strength vs. compressive strength: comparison of measured strengths and predicted strengths

The multivariable nonlinear regression model, based on the power model, that correlates the splitting tensile strength and steel fiber content with the flexural strength is

$$f_r = 0.083(f_{st})^{1.246}(1 + 0.162(V_f)) + 664 \qquad \text{(Eq. 4.3.2.2)}$$

where,

$f_r = flexural\ strength$ (psi)

$f_{st} = splitting\ tensile\ strength$ (psi) and

$V_f = volumetric\ steel\ fiber\ content$ (%)

The constants that are incorporated into Eq. 4.3.2.2 were derived from regression analysis. Figure 4.3.2.2 shows that there is a correlation between the flexural strength, splitting tensile strength, and steel fiber content. The predicted flexural values produced by Eq. 4.3.2.2 trend with the measured flexural strengths resulting in a model that predicts realistic strengths. The RMSE is 635.8 psi and the coefficient of determination is 0.74 for Eq. 4.3.2.2. This poor correlation is

potentially due to the failure characteristics observed in the splitting tensile tests of J3-UHPC specimens. Increasing the fiber content in the splitting tensile specimens resulted in splitting tensile failures that were not completely in indirect tension. It was observed that the splitting tensile tests of 4% and 6% steel fiber content specimens experienced indirect tension before the first crack and a combined compressive-tensile stress after the first crack. Furthermore, crushing of the UHPC at the top and bottom of the specimen was observed during steel fiber bridging. Consequentially, the splitting tensile strength of J3-UHPC specimens with high steel fiber contents is not representative of the true indirect tensile strength.

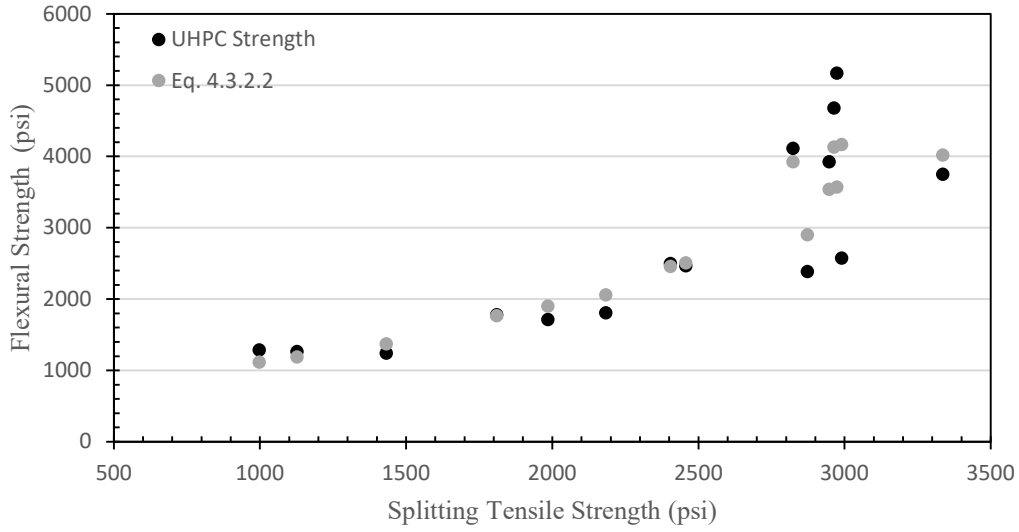

Figure 4.3.2. 2 Flexural strength vs. splitting tensile strength: comparison of measured strengths and predicted strengths

The multivariable nonlinear regression model, based on the power model, that correlates the direct tensile post-cracking strength and steel fiber content with the flexural strength is

$$f_r = 2.05\text{x}10^{-5}\left(f_{pc}\right)^{2.55}(1 + 0.046(V_f)) + 685 \qquad \text{(Eq. 4.3.2.3)}$$

where,

$f_r = flexural\ strength$ (psi)

$f_{pc} =$ direct tensile post cracking $strength$ (psi) and

$V_f = volumetric\ steel\ fiber\ content$ (%)

The constants that are incorporated into Eq. 4.3.2.3 were derived from regression analysis. Figure 4.3.2.3 shows that there is a strong correlation between the flexural strength, direct tensile post-cracking strength, and steel fiber content. The predicted flexural values produced by Eq. 4.3.2.3 trend accurately with the measured flexural strengths resulting in a model that predicts realistic strengths. The RMSE is 331.9 psi and the coefficient of determination is 0.93 for Eq. 4.3.2.3.

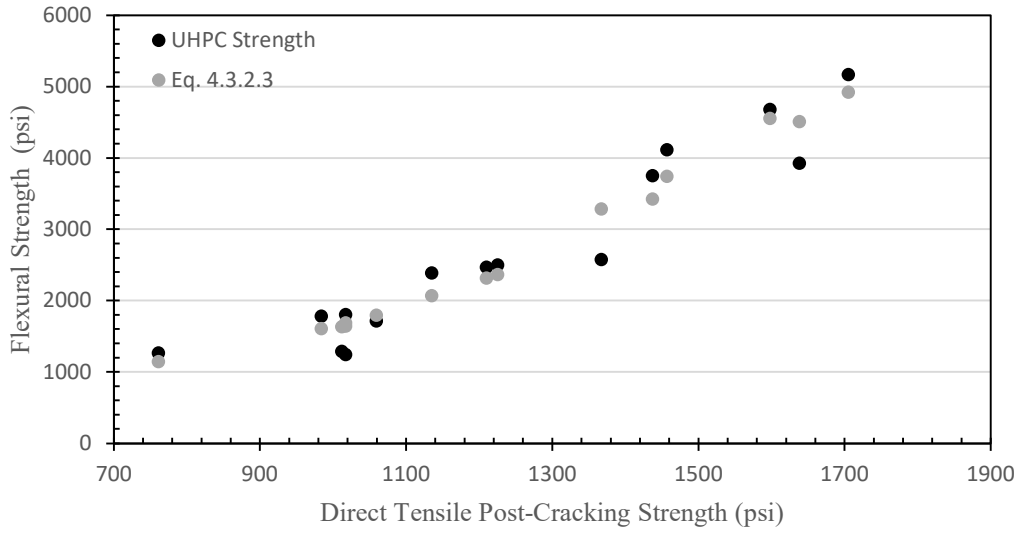

Figure 4.3.2. 3 Flexural strength vs. direct tensile post-cracking strength: comparison of measured strengths and predicted strengths

The multivariable nonlinear regression model, based on the power model, that correlates the direct tensile first crack strength and steel fiber content with the flexural strength is

$$f_r = 9.92\text{x}10^{-9}\left(f_{fc}\right)^{3.129}(1 + 21.425(V_f)) + 1{,}169 \qquad \text{(Eq. 4.3.2.4)}$$

where,

$f_r = flexural\ strength$ (psi)

$f_{fc} = direct\ tensile\ first\ crack\ strength$ (psi) and

$V_f = volumetric\ steel\ fiber\ content$ (%)

The constants that are incorporated into Eq. 4.3.2.4 were derived from regression analysis. Figure 4.3.2.4 shows that there is a strong correlation between the flexural strength, direct tensile first crack strength, and steel fiber content. The predicted flexural values produced by Eq. 4.3.2.4 trend accurately with the measured flexural strengths resulting in a model that predicts realistic strengths. The RMSE is 345.4 psi and the coefficient of determination is 0.92 for Eq. 4.3.2.4. The root mean square error and R^2 (coefficient of determination) analysis is shown in Table 4.3.2. 1.

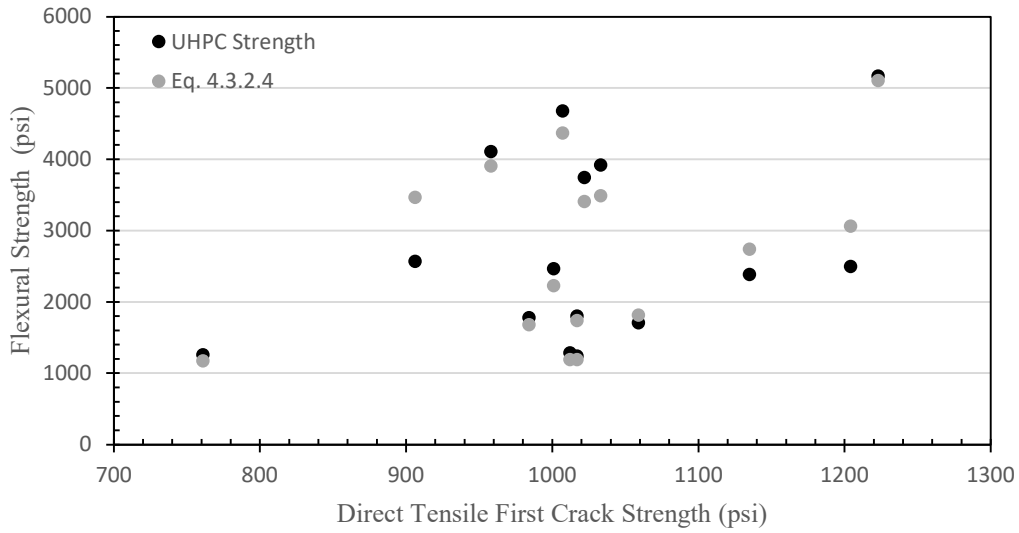

Figure 4.3.2. 4 Flexural strength vs. direct tensile first crack strength: comparison of measured strengths and predicted strengths

Table 4.3.2. 1 Flexural strength root mean square error analysis

Equation	RMSE	R^2
Eq. 4.3.2.1	525.2	0.82
Eq. 4.3.2.2	635.8	0.74
Eq. 4.3.2.3	331.9	0.93
Eq. 4.3.2.4	345.4	0.92

Note: RMSE = root mean square error (psi), R^2 = coefficient of determination

4.3.3 Direct Tensile Post-Cracking Strength Correlations

The multivariable nonlinear regression model, based on the power model, that correlates the compressive strength and steel fiber content with the direct tensile post-cracking strength is

$$f_{pc} = 2.83\text{x}10^{6}(f_c)^{-2.51}(1 + 3.8\text{x}10^{6}(V_f)) + 875 \qquad \text{(Eq. 4.3.3.1)}$$

where,

$f_{pc} = direct\ tensile\ post\ cracking\ strength\ (psi)$

$f_c = compressive\ strength$ (psi) and

$V_f = volumetric\ steel\ fiber\ content$ (%)

The constants that are incorporated into Eq. 4.3.3.1 were derived from regression analysis. Figure 4.3.3.1 shows that there is a correlation between the direct tensile post-cracking strength, compressive strength, and steel fiber content. The predicted direct tensile post-cracking values produced by Eq. 4.3.3.1 trend accurately with the measured direct tensile post-cracking strengths resulting in a model that predicts realistic strengths. The RMSE is 113.8 psi and the coefficient of determination is 0.82 for Eq. 4.3.3.1.

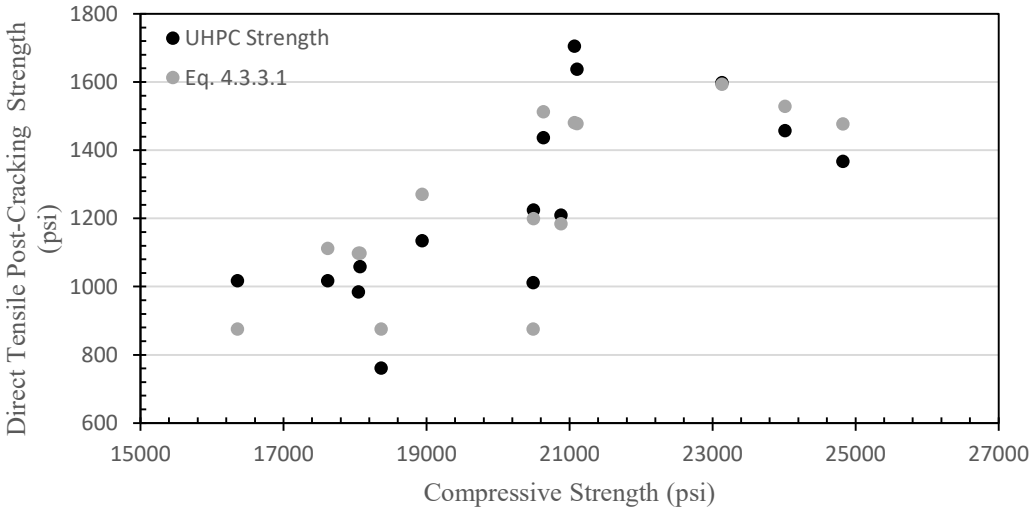

Figure 4.3.3. 1 Direct tensile post-cracking strength vs. compressive strength: comparison of measured strengths and predicted strengths

The multivariable nonlinear regression model, based on the power model, that correlates the flexural strength and steel fiber content with the direct tensile post-cracking strength is

$$f_{pc} = 24.39(f_r)^{0.476}(1 + 0.012(V_f)) + 183 \qquad \text{(Eq. 4.3.3.2)}$$

where,

$f_{pc} = direct\ tensile\ post\ cracking\ strength\ (psi)$

$f_r = flexural\ strength$ (psi) and

$V_f = volumetric\ steel\ fiber\ content\ (\%)$

The constants that are incorporated into Eq. 4.3.3.2 were derived from regression analysis. Figure 4.3.3.2 shows that there is a strong correlation between the direct tensile post-cracking strength, flexural strength, and steel fiber content. The predicted direct tensile post-cracking values produced by Eq. 4.3.3.2 trend accurately with the measured direct tensile post-cracking strengths resulting in a model that predicts realistic strengths. The RMSE is 79.7 psi and the coefficient of determination is 0.91 for Eq. 4.3.3.2.

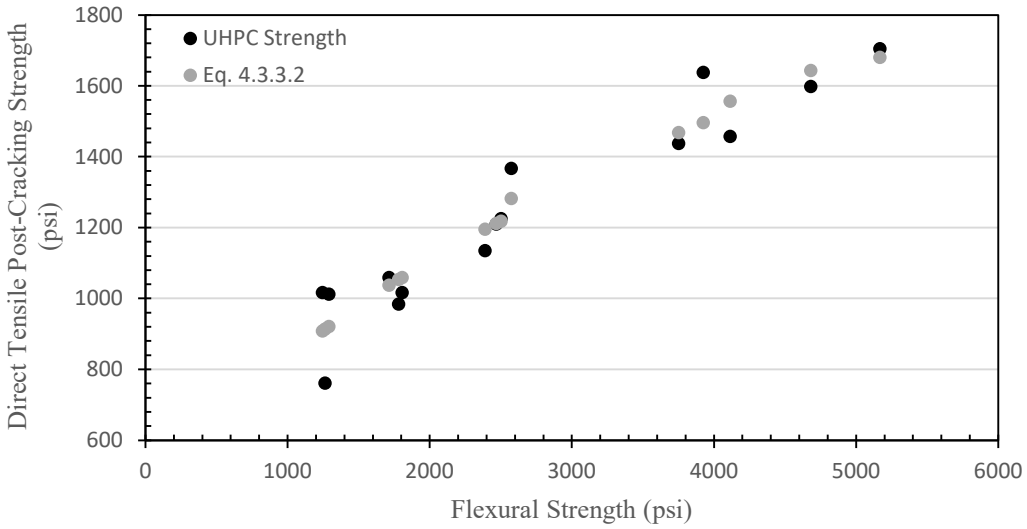

Figure 4.3.3. 2 Direct tensile post-cracking strength vs. flexural strength: comparison of measured strengths and predicted strengths

The multivariable nonlinear regression model, based on the power model, that correlates the splitting tensile strength and steel fiber content with the direct tensile post-cracking strength is

$$f_{pc} = 0.024(f_{st})^{1.213}(1 + 0.158(V_f)) + 783 \qquad \text{(Eq. 4.3.3.3)}$$

where,

$f_{pc} = direct\ tensile\ post\ cracking\ strength\ (psi)$

$f_{st} = splitting\ tensile\ strength$ (psi) and

$V_f = volumetric\ steel\ fiber\ content$ (%)

The constants that are incorporated into Eq. 4.3.3.3 were derived from regression analysis. Figure 4.3.3.3 shows that there is a correlation between the direct tensile post-cracking strength, splitting tensile strength, and steel fiber content. The predicted direct tensile post-cracking values produced by Eq. 4.3.3.3 trend accurately with the measured direct tensile post-cracking strengths

resulting in a model that predicts realistic strengths. The RMSE is 128.3 psi and the coefficient of determination is 0.78 for Eq. 4.3.3.3.

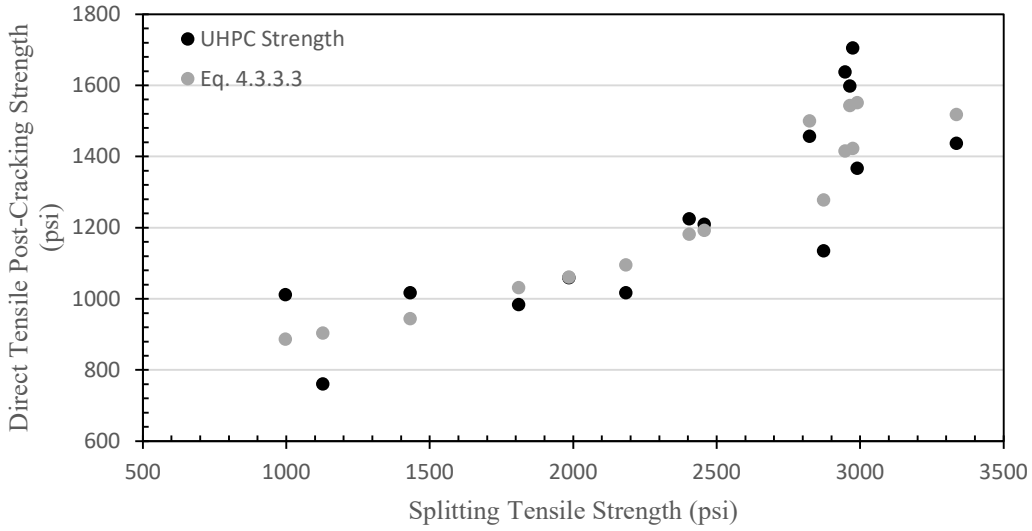

Figure 4.3.3. 3 Direct tensile post-cracking strength vs. splitting tensile strength: comparison of measured strengths and predicted strengths

The multivariable nonlinear regression model, based on the power model, that correlates the direct tensile first crack strength and steel fiber content with the direct tensile post-cracking strength is

$$f_{pc} = 3.75\text{x}10^{-4}\left(f_{fc}\right)^{1.918}(1 + 0.522(V_f)) + 711 \qquad \text{(Eq. 4.3.3.4)}$$

where,

$f_{pc} = direct\ tensile\ post\ cracking\ strength\ (psi)$

$f_{fc} = direct\ tensile\ first\ crack\ strength$ (psi) and

$V_f = volumetric\ steel\ fiber\ content\ (\%)$

The constants that are incorporated into Eq. 4.3.3.4 were derived from regression analysis. Figure 4.3.3.4 shows that there is a strong correlation between the direct tensile post-cracking

strength, direct tensile first crack strength, and steel fiber content. The predicted direct tensile post-cracking values produced by Eq. 4.3.3.4 trend accurately with the measured direct tensile post-cracking strengths resulting in a model that predicts realistic strengths. The RMSE is 89.0 psi and the coefficient of determination is 0.89 for Eq. 4.3.3.4. The root mean square error and R^2 (coefficient of determination) analysis is shown in Table 4.3.3.1.

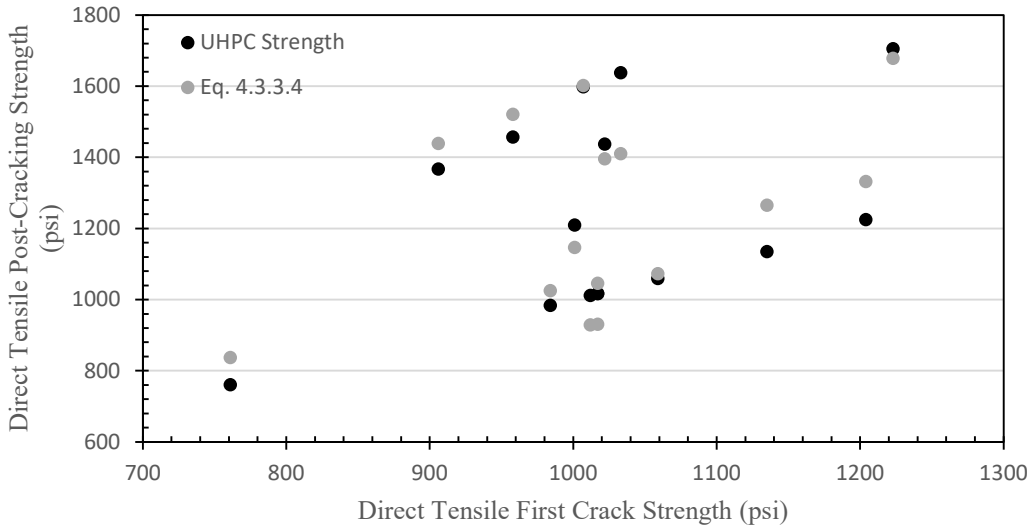

Figure 4.3.3. 4 Direct tensile post-cracking strength vs. direct tensile first crack strength: comparison of measured strengths and predicted strengths

Table 4.3.3. 1 Direct tensile post-cracking strength root mean square error analysis

Equation	**RMSE**	**R^2**
Eq. 4.3.3.1	113.8	0.82
Eq. 4.3.3.2	79.9	0.91
Eq. 4.3.3.3	128.3	0.78
Eq. 4.3.3.4	89.0	0.89

Note: RMSE = root mean square error (psi), R^2 = coefficient of determination

4.3.4 Direct Tensile First Crack Strength Correlations

The multivariable nonlinear regression model, based on the power model, that correlates the compressive strength and steel fiber content with the direct tensile first crack strength is

$$f_{fc} = 2.8\text{x}10^{15}(f_c)^{-6.8}(1 + 3.4\text{x}10^{15}(V_f)) + 926 \qquad \text{(Eq. 4.3.4.1)}$$

where,

$f_{fc} = direct\ tensile\ first\ crack\ strength$ (psi)

$f_c = compressive\ strength$ (psi) and

$V_f = volumetric\ steel\ fiber\ content$ (%)

The constants that are incorporated into Eq. 4.3.4.1 were derived from regression analysis. Figure 4.3.4.1 shows that there is a weak correlation between the direct tensile first crack strength, compressive strength, and steel fiber content. The predicted direct tensile first crack values produced by Eq. 4.3.4.1 trends poorly with the measured direct tensile first crack strengths resulting in a model that predicts unrealistic strengths. The RMSE is 92.6 psi and the coefficient of determination is 0.27 for Eq. 4.3.4.1.

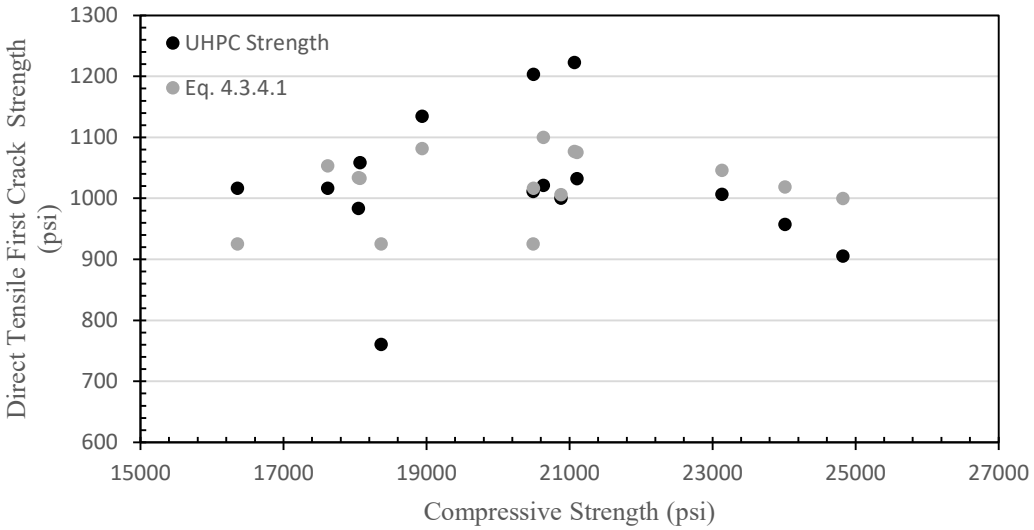

Figure 4.3.4. 1 Direct tensile first crack strength vs. compressive strength: comparison of measured strengths and predicted strengths

The multivariable nonlinear regression model, based on the power model, that correlates the flexural strength and steel fiber content with the direct tensile first crack strength is

$$f_{fc} = 0.45(f_r)^{0.886}(1 - 0.109(V_f)) + 708 \qquad \text{(Eq. 4.3.4.2)}$$

where,

$f_{fc} = direct\ tensile\ first\ crack\ strength$ (psi)

$f_r = flexural\ strength$ (psi) and

$V_f = volumetric\ steel\ fiber\ content$ (%)

The constants that are incorporated into Eq. 4.3.4.2 were derived from regression analysis. Figure 4.3.4.2 shows that there is a weak correlation between the direct tensile first crack strength, flexural strength, and steel fiber content. The predicted direct tensile first crack values produced by Eq. 4.3.4.2 trend poorly with the measured direct tensile first crack strengths resulting in a model that predicts unrealistic strengths. The RMSE is 76.5 psi and the coefficient of determination is 0.50 for Eq. 4.3.4.2.

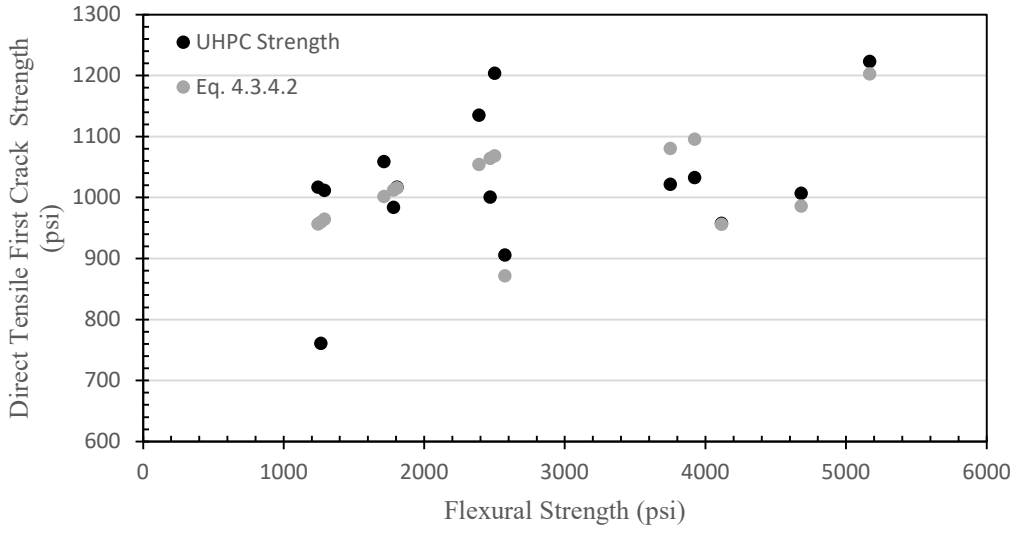

Figure 4.3.4. 2 Direct tensile first crack strength vs. flexural strength: comparison of measured strengths and predicted strengths

The multivariable nonlinear regression model, based on the power model, that correlates the splitting tensile strength and steel fiber content with the direct tensile first crack strength is

$$f_{fc} = 0.005(f_{st})^{1.417}(1 - 0.108(V_f)) + 875 \qquad \text{(Eq. 4.3.4.3)}$$

where,

$f_{fc} = direct\ tensile\ first\ crack\ strength$ (psi)

$f_{st} = splitting\ tensile\ strength$ (psi) and

$V_f = volumetric\ steel\ fiber\ content$ (%)

The constants that are incorporated into Eq. 4.3.4.3 were derived from regression analysis. Figure 4.3.4.3 shows that there is a weak correlation between the direct tensile first crack strength, splitting tensile strength, and steel fiber content. The predicted direct tensile first crack values produced by Eq. 4.3.4.3 trend poorly with the measured direct tensile first crack strengths resulting in a model that predicts unrealistic strengths. The RMSE is 85.4 psi and the coefficient of determination is 0.39 for Eq. 4.3.4.3.

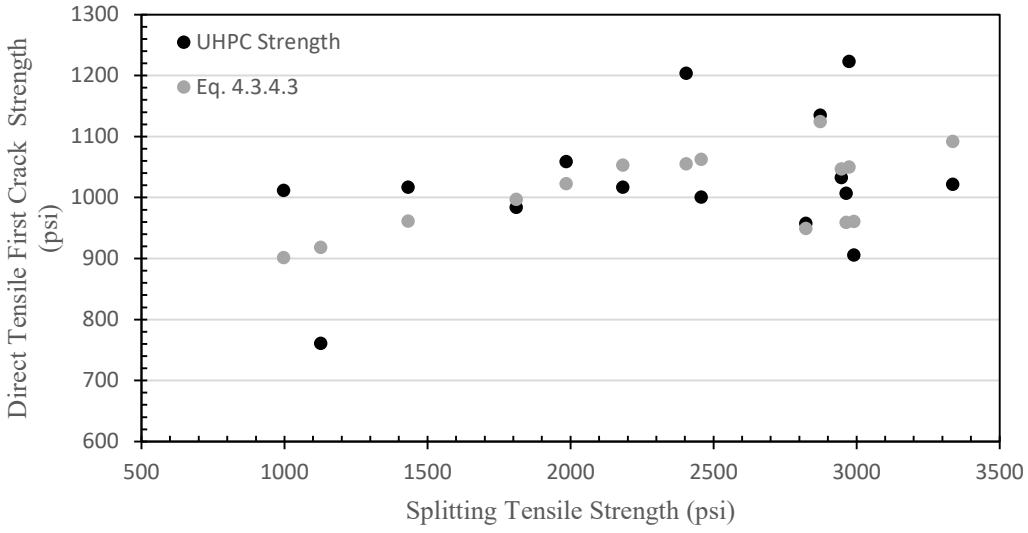

Figure 4.3.4. 3 Direct tensile first crack strength vs. splitting tensile strength: comparison of measured strengths and predicted strengths

The multivariable nonlinear regression model, based on the power model, that correlates the direct tensile post-cracking strength and steel fiber content with the direct tensile first crack strength is

$$f_{fc} = 176\left(f_{pc}\right)^{0.354}\left(1 - 0.028(V_f)\right) - 1000 \qquad \text{(Eq. 4.3.4.4)}$$

where,

$f_{fc} = direct\ tensile\ first\ crack\ strength$ (psi)

$f_{pc} = direct\ tensile\ post\ cracking\ strength\ (psi)\ and$

$V_f = volumetric\ steel\ fiber\ content$ (%)

The constants that are incorporated into Eq. 4.3.4.4 were derived from regression analysis. Figure 4.3.4.4 shows that there is a weak correlation between the direct tensile first crack strength, direct tensile post-cracking strength, and steel fiber content. The predicted direct tensile first crack values produced by Eq. 4.3.4.4 trend poorly with the measured direct tensile first crack strengths resulting in a model that predicts unrealistic strengths. The RMSE is 67.9 psi and the coefficient of determination is 0.62 for Eq. 4.3.4.4. The root mean square error and R^2 (coefficient of determination) analysis is shown in Table 4.3.4.1.

The direct tensile first crack stress was shown to be a difficult strength to predict. Further testing and analysis is required to properly determine an appropriate mathematical model that is capable of correlating the direct tensile first crack strength with other mechanical properties. The power model used in this study is not adequate for predicting the direct tensile first crack strength. Parameters, in addition to the mechanical strengths and steel fiber content, such as cementitious material components and HRWR should be considered as potential factors that affect the first crack strength of UHPC.

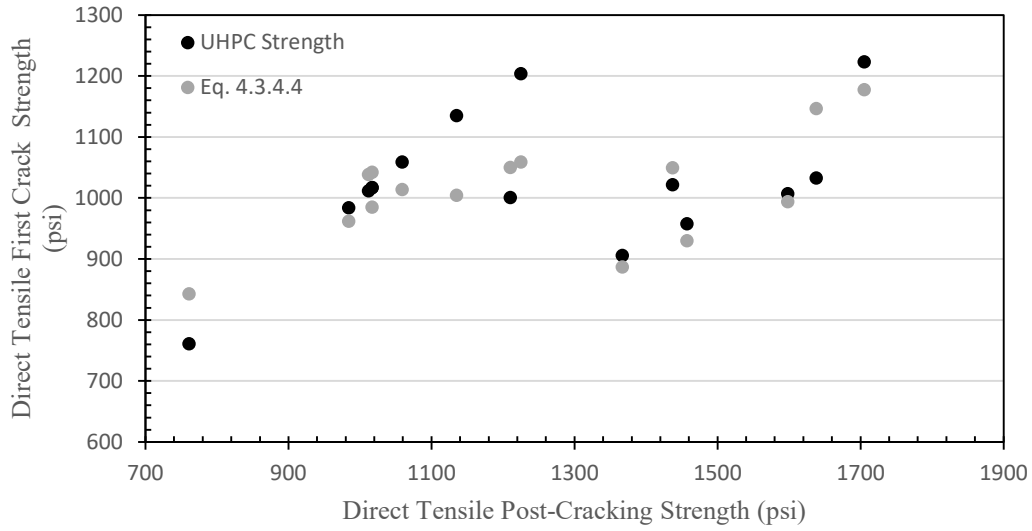

Figure 4.3.4. 4 Direct tensile first crack strength vs. direct tensile post-cracking strength: comparison of measured strengths and predicted strengths

Table 4.3.4. 1 Direct tensile first crack strength root mean square error analysis

Equation	**RMSE**	**R^2**
Eq. 4.3.4.1	92.6	0.27
Eq. 4.3.4.2	76.5	0.50
Eq. 4.3.4.3	85.4	0.39
Eq. 4.3.4.4	67.9	0.62

Note: RMSE = root mean square error (psi), R^2 = coefficient of determination

4.4 Comparison of UHPC, High Strength Concrete, and Normal Strength Concrete Models

The power regression model that correlates the flexural and compressive strengths of normal strength concrete is (Campos et al. 2020):

$$f_r = 5.73 f_c^{0.564} \qquad \text{(Eq. 4.4.1)}$$

where,

$f_r = flexural\ strength\ (psi)$ (modulus of rupture) *and*

$f_c = compressive\ strength\ (psi)$

The power regression model that correlates the splitting tensile and compressive strengths of high-strength concrete is:

$$f_{st} = 0.968 f_c^{0.735} \qquad \text{(Eq. 4.4.2)}$$

where,

$f_{st} = splitting\ tensile\ strength\ (psi)$ (indirect tensile) and

$f_c = compressive\ strength\ (psi)$

Eqs. 4.4.1 and 4.4.2 trend well with the measured strengths, which is seen in Table 4.4.1. Comparatively, the UHPC multivariable nonlinear regression models produce more accurate and realistic predictions for both correlations. This is due to the incorporation of the steel fiber content in the UHPC regression models. This suggests that the correlations between the mechanical properties of UHPC are strongly influenced by the addition of steel fibers. Eqs. 4.4.1 and 4.4.2 performed poorly when predicting UHPC compressive and splitting tensile strengths.

Table 4.4. 1 Normal and high-strength root mean square error analysis

Equation	**RMSE**
Eq. 4.4.1	38.3
Eq. 4.4.2	33.5

Note: RMSE = root mean square error (psi)

5 Summary, Conclusions, and Recommendations

5.1 Summary

The present study used varying steel fiber contents as well as direct tensile, splitting tensile, compressive and flexural strengths of 60 specimens to develop preliminary empirical models that correlate the direct tensile first crack strength, maximum post-cracking strength, and fiber content with the splitting tensile, flexural (modulus of rupture), and compressive strengths at 28 days for non-proprietary UHPC. The accuracy of the developed models was verified by comparing their predictive capabilities with the measured strengths obtained from the laboratory tests.

Literature was surveyed to determine significant information related to this study to develop an advanced understanding of non-proprietary UHPC and correlation modeling. The laboratory experiments that were conducted in this study include flowability, compressive strength, and direct tensile strength tests. Steel fiber contents of 0%, 1%, 2%, 4%, and 6% were considered in this study. Statistical analysis software was used to analyze the strength test results and develop regression models. The root mean square error method was used to analyze the accuracy between the values predicted by the regression models and the measured laboratory values.

The approach and methods consisted of experimental procedures for constructing, curing, and testing 15 non-proprietary UHPC prismatic specimens of varying fiber contents, development of a direct tensile test assembly that closely matches that used by Graybeal and Baby (2013), examination of existing strength data (splitting tensile and flexural), and correlation model development.

5.2 Conclusions

From the direct tensile tests and regression analysis, the following conclusions can be made about the effect of fiber content on the tensile strength of non-proprietary UHPC:

- Steel fiber content has a weak effect on the direct tensile first crack strength of J3-UHPC. From the average stress-strain curves of 0%, 1%, 2%, 4%, and 6% steel fiber content, the direct tensile first crack strength generally occurred at the end of the elastic region where steel fiber content was observed to have a weak effect on the strength.
- Steel fiber content has a strong effect on the direct tensile maximum post-cracking strength of J3-UHPC. The direct tensile post-cracking strength generally increases as the steel fiber content increases. A steel fiber content of 6% was the only fiber content observed to not follow this trend, likely due to poor fiber distribution and consolidation.
- Steel fiber content affects the splitting tensile, flexural, and direct tensile post-cracking strengths of J3-UHPC similarly. Due to the presence of steel fibers, the tensile and indirect tensile strengths exhibit similar trends in strength. The direct tensile strength decrease in 6% steel fiber content is also observed in the splitting tensile and flexural strengths.
- Steel fiber content affects the compressive strength differently than the direct or indirect tensile strengths of J3-UHPC. The compressive strength generally increases linearly with increasing steel fiber content. Poor fiber distribution does not impact the compressive strength to the same degree as the direct and indirect tensile strengths.
- Steel fiber content has a strong effect on the cracking pattern of direct tensile J3-UHPC specimens. The cracking patterns seen in the specimens appear to be dictated by the fiber distribution within the specimen. 0% and 1% steel fiber specimens cracked similarly. 2%,

4%, and 6% steel fiber specimens developed multiple cracks until a localized crack formed. 6% steel fiber specimens experienced unique cracks during the strain hardening region.

- The 4% steel fiber J3-UHPC specimens attained the largest maximum direct tensile post-cracking, flexural, and splitting tensile strengths.
- Steel fiber content has a strong effect on the average stress-strain curve of J3-UHPC. Two average stress-strain curves were observed. The average stress-strain curves for the steel fiber contents of 0% and 1% lacked the strain hardening region that is present in the average stress-strain curves of the steel fiber contents of 2%, 4%, and 6%.
- The compressive strength has a strong correlation with the direct and indirect tensile strengths of J3-UHPC. From the regression modeling it was determined that the compressive strength had the strongest correlation with all of the direct and indirect tensile strengths.
- The multivariable nonlinear power model was able to predict the mechanical strengths of J3-UHPC with R^2 values ranging from 0.27 to 0.93. The splitting tensile strength correlations had R^2 values ranging from 0.81 to 0.93. The flexural strength correlations had R^2 values ranging from 0.78 to 0.93. The direct tensile maximum post-cracking strength correlations had R^2 values ranging from 0.78 to 0.91. The direct tensile first crack strength correlations had R^2 values ranging from 0.27 to 0.62.
- Steel fiber content has a significant impact on the predictive capabilities of the power model. Because the steel fiber content has a significant impact on the direct and indirect tensile strengths, the steel fiber content must be incorporated in the regression models in order to produce realistic results.

- The idealized average stress-strain curves represent the measured stress-strain curves of J3-UHPC. The idealized average stress-strain curves were derived from the measured average stress-strain curves of 0%, 1%, 2%, 4%, and 6% steel fiber content.
- There is no correlation between the compressive, splitting tensile, and flexural strength models of J3-UHPC, normal strength concrete, and high-strength concrete. The poor correlation is due to the absence of steel fibers in the normal and high-strength concrete regression modeling.

5.3 Recommendations

From the conclusions and results, the following recommendations are made:

- The idealized average stress-strain curves should be considered as an aid for the design of non-proprietary J3-UHPC structures that will experience large tensile stresses. The direct tensile first crack stress can be taken as 930 psi, which is the average direct tensile first crack stress of the 0% steel fiber specimens. This first crack stress was chosen due to there only being a 17% increase in first crack strength between 0% and 4% steel fiber contents. The post-cracking stress can be determined by correlating the direct tensile post-cracking strength with the flexural strength and steel fibers with regression Eq. 4.3.3.2. Although the preliminary idealized average stress-strain curves can be used as a design aid, further analysis of the true strain hardening and softening should be considered to create accurate idealized average stress-strain curves for J3-UHPC.
- The cementitious components of J3-UHPC and the HRWR should be considered in future regression modeling to develop models that accurately predict the direct tensile first crack strength.
- Future testing should use larger sample sizes to further refine the regression models.

- Future modeling should consider other non-proprietary UHPC mixes as well as data from previous research to further refine the correlation models.
- Further testing of 6% steel fiber content is necessary to determine the effects of steel fiber distribution on the cracking patterns and strengths of UHPC.

References

Ahmed, M., El Hadi, K. M., Hasan, M. A., Mallick, J., and Ahmed, A. 2014. "Evaluating the co-relationship between concrete flexural tensile strength and compressive strength." Int. J. of Stru. Eng., 5 (2), 115–131. http://dx.doi.org/10.1504/IJSTRUCTE.2014.060902

ACI (American Concrete Institute). 2014. Building code requirements for structural concrete and commentary. ACI 318-2014. Farmington Hills, MI: ACI.

ACI Committee 363. 2010. *Report on high-strength concrete*. ACI 363R-10, American Concrete Institute Committee 363, Farmington Hills, MI: ACI.

ASCE (American Society of Civil Engineers). 2017. "2017 Infrastructure Report Card." ASCE's 2017 Infrastructure Report Card. Accessed March 21, 2020. https://www.infrastructurereportcard.org/cat-item/roads/.

ASTM (American Society for Testing and Materials). 2018a, Standard test method for compressive strength of cylindrical concrete specimens. C39/C39M – 18, West Conshohocken, PA.

ASTM (American Society for Testing and Materials). 2017, Standard test method for fabricating and testing specimens of ultra-high performance concrete. C1856/C1856M – 17, West Conshohocken, PA.

ASTM (American Society for Testing and Materials). 2019, Standard test method for flexural performance of fiber-reinforced concrete (using beam with third-point loading). C1609/C1609M – 19a, West Conshohocken, PA.

ASTM (American Society for Testing and Materials). 2018b, Standard Test Method for Splitting Tensile Strength of Cylindrical Concrete Specimens. C496/C496M − 17, West Conshohocken, PA.

Campos, R., Mendez Larrain, M.M., Zaman, M. et al. 2020. "Relationships between compressive

and flexural strengths of concrete based on fresh field properties." Int. J. Pavement Res. Technol. https://doi.org/10.1007/s42947-020-1074-0

Amudhavalli, N.K. and Poovizhiselvi, M., 2017. "Relationship between compressive strength and flexural strength of polyester fiber reinforced concrete." Int. J. of Eng. Trends and Technology., 45 (4), 158-160. https://doi.org/10.14445/22315381/IJETT-V45P234

De la Varga I., El-Helou R., Graybeal B. A., Haber Z. B., and Nakashoji B., 2018. Properties and Behavior of UHPC-Class Materials. FHWA-HRT-18-036, Mclean, Virginia.

Dyachkova, Y. 2020.. Effect of Steel Fiber Content on Mechanical Properties of Non-proprietary Ultra-High Performance Concrete. M.S. Thesis, University of Oklahoma, Norman, OK.

Esquinas, A. R., Ramos, C., Jiménez, J. R., Fernández, J. M., and de Brito, J. 2016. "Mechanical behaviour of self-compacting concrete made with recovery filler from hot-mix asphalt plants." Const. and Building Materials., 131, 114-128. https://doi.org/10.1016/j.conbuildmat.2016.11.063

Graybeal, B. A., & Baby, F., 2013. Development of Direct Tension Test Method for Ultra-High-Performance Fiber-Reinforced Concrete. ACI Materials Journal, 110(2). doi: 10.14359/51685532

Hammitt, G. M. 1974. Concrete strength relationships, U.S. Vicksburg, Miss: Army Engineer Waterways Experiment Station, Soils and Pavements Laboratory.

Le Hoang, An and Fehling, Ekkehard. 2017. "Influence of Steel Fiber Content and Aspect Ratio on The Uniaxial Tensile and Compressive Behavior of Ultra High Performance Concrete." 2017. Construction and Building Materials, 153, 790-806, ISSN: 09500618; DOI: 10.1016/j.conbuildmat.2017.07.130

Lane, D. S. 1988. Evaluation of concrete characteristics for rigid pavements. Charlottesville, VA:

Virginia Transportation Research Council.

Looney, T., McDaniel, A., Volz, J., Floyd, R. 2019. “Development and Characterization of Ultra-High Performance Concrete with Slag Cement for Use as Bridge Joint Material.” British Journal of Civil and Architecture Engineering, 1(2), 14 pp.

Pul, Selim. 2008. “Experimental investigation of tensile behavior of high strength concrete.” Indian J. of Eng. and Material Sci., 15 (6), 467-472.

Ramadoss, P. 2014 “Correlation of compressive strength and other engineering properties of high-performance steel fiber–reinforced concrete.” J. Materials Civ. Eng., 27 (1), 04014114. https://doi.org/10.1061/(ASCE)MT.1943-5533.0001050

Raphael, J. M. 1984. “Tensile strength of concrete.” ACI Journal., 81 (2), 158-165.

Russell H. G. and Graybeal, B. A., 2013. Ultra-high performance concrete: a state-of-the-art reportfor the bridge community. FHWA-HRT-13-060, Mclean, Virginia.

Taylor, P., Van Dam, T., Sutter, L., and Fick, G. 2019. “Integrated Materials and Construction Practices for Concrete Pavement: A State-of-the-Practice Manual.” Institute for Transportation Iowa State University. Accessed Feb 21, 2020. https://intrans.iastate.edu/app/uploads/2019/05/IMCP_manual.pdf.

TRIP. 2019. “National Fact Sheet.” TRIP. Accessed March 23, 2020. http://www.tripnet.org/docs/Fact_Sheet_National.pdf.

U.S. Department of Transportation. 2015. “2015 Status of the Nation’s Highways, Bridges and Transit: Conditions and Performance.” Federal Highway Administration/ Department of Transportation. Accessed March 23, 2020. https://www.fhwa.dot.gov/policy/2015cpr/pdfs.cfm.

Wu, Zemei, et al. Effects of Steel Fiber Content And Shape on Mechanical Properties of Ultra-

High Performance Concrete. 2015. Construction and Building Materials, 103, 8-14; ISSN: 09500618; DOI: 10.1016/j.conbuildmat.2015.11.028;

Xu, B.W. and Shi, H. S. 2009. “Correlations among mechanical properties of steel fiber reinforced concrete.” Const. and Building Materials., 23 (12), 3468-3474. https://doi.org/10.1016/j.conbuildmat.2009.08.017